Geological Survey of Israel
Ministry of Energy

Air-sea heat exchange in the desert semi-enclosed Gulf of Eilat (Aqaba)

Shai Abir



Report GSI 11 2023

August 2023

©Published by the Geological Survey of Israel
32 Yeshayahu Leibowitz St. Jerusalem 9692100, Israel

Front picture:
The fringing coral reef of the Gulf of Eilat (Aqaba). Looking north from the Under Water Observatory of Eilat tower. Picture was taken by Shai Abir.

Back pictures:
1. The fringing coral reef of the Gulf of Eilat (Aqaba). Picture was taken by TerraScan.
2. Schematic representation of the mean energy partitioning at the Gulf of Eilat (Aqaba) during the 2-year observation period (values are given W m^{-2}). The mean annual surface energy loss is represented by Q_{SWR}, it is balanced by heat advection Q_A through the northbound currents. Credit: Yoav Balaban
3. The Eddy Covariance tower installed on the Inter University Institute for Marine Sciences in Eilat. Measuring the surface gas, energy, and momentum fluxes between the Atmosphere and the surface of the sea.
   Picture was taken by Yonatan Shaked.

Design: Tirza Tzuberi

Geological Survey of Israel
Ministry of Energy

Air-sea heat exchange in the desert semi-enclosed Gulf of Eilat (Aqaba)

Shai Abir

Thesis for the degree of "Master of Science"

submitted to the Hebrew University of Jerusalem.

The study was carried out under the supervision of:

Prof. Nadav G. Lensky, Geological Survey of Israel.

Prof. Efrat Morin, Hebrew University of Jerusalem.

Prof. Hamish A. McGowan, The University of Queensland.

Report GSI/11/2023 August 2023

Acknowledgments

Thanks to Prof. Nadav Lensky, Prof. Efrat Morin, and Prof. Hamish McGown for their dedicated and constructive mentoring and contribution to this research and my development. Thanks to Dr. Yonatan Shaked and Prof. Hezi Gildor for their imperative contribution to this research. Thanks to the team from the Geological Survey of Israel; Uri Malik, Guy Tau, Haggi Eyal, and Ziv Mor. Yoav Balaban for the graphic illustration. Thanks to my colleagues in the Hydrometeorological lab of the Earth Science Institute. Asaph Rivlin, Modi Pilersdorf, the Israel National Monitoring Program at the Gulf of Eilat, and The Interuniversity Institute for Marine Sciences in Eilat for access to infrastructure and services. Dr. Assaf Zvuloni and Chen Toufikian of Israel's Nature and Parks Authority for their assistance. Thanks to Prof. Pinhas Alpert and Prof. Hadas Saaroni Lab for giving us access to their daily synoptic classification dataset. The University of Queensland for the financial and technical support of the research. The research was supported by the Israel Science Foundation (Grant ISF-2018/1471), PI–NGL, and by Funds for PIs EM, HM, and NGL from the Hebrew University of Jerusalem–Zelman Cowen Academic Initiatives (ZCAI) Joint Projects 2021 (2022-2024). HG was supported by a grant from the Ministry of Science and Technology.

1 Abstract

Research of the air-sea exchange of heat, gas, and momentum through surface fluxes, provides valuable insights into the physical and chemical processes of marine environments. These exchange fluxes affect the climate, ocean circulation processes, and the marine biological environment thermoregulation processes.

This study aims to accurately quantify heat exchange fluxes in the Gulf of Eilat. In addition, to determine evaporation rate and associated micrometeorology, and analyze the relationship between wind speed, vapor pressure difference, evaporation rates, and their diurnal to seasonal cycles. The research also investigates the error in bulk formulae for evaporation in stable atmospheric conditions in the Gulf of Eilat. Furthermore, it evaluates the net energy exchange and heat budget of the surface water, primarily through evaporation, and examines the contribution of heat advection to the overall heat budget, providing insights into the dynamics of the Gulf of Eilat. The study also explores the impact of wintertime atmospheric circulation on heat loss and water column vertical mixing in the Gulf of Eilat.

To achieve these objectives, a 2-year study was conducted utilizing Eddy Covariance measurements of air-sea exchange fluxes in the Gulf of Eilat. The energy balance approach was employed to quantify the complete energy partitioning of the water surface and water column.

The findings reveal that the mean evaporation rate in the Gulf of Eilat is 3.22 m $year^{-1}$, surpassing previous estimates derived from bulk formulae and the radiation heat flux to the arid semi-enclosed sea. The parameterization of the atmospheric boundary layer stability is identified as the main cause of evaporation error in stable atmospheric conditions using bulk formulae. The evaporation rate exhibits a peak during summer, contrary to previous estimations which stated peak evaporation during winter. The lowest evaporation rate occurs during winter (8.01 mm day^{-1}) due to reduced wind speed. Conversely, higher wind speeds during spring, summer, and autumn, accompanied by an afternoon increase in vapor pressure difference due to higher water temperature and lower humidity, result in a higher mean evaporation rate of 9.08 mm day^{-1}.

The analysis demonstrates that there is a net cooling effect on the surface water (-79 W m^{-2}) primarily through evaporation throughout most of the year, with a small net energy gain observed during summer. The findings suggest that the air-sea heat flux alone cannot account

for the seasonal heating of the Gulf water, as indicated in previous studies. The significant heat deficit is compensated by the advection of heat via the northbound currents from the Red Sea, indirectly quantified through energy balance considerations.

Moreover, the study provides a deeper understanding of the synoptic scale forcing on the energy balance through extreme heat loss events. These events significantly cool and increase salinity of the surface water through sensible and latent heat consequently, destabilizing the water column. Indicating the importance of these processes to winter water column vertical mixing in the Gulf of Eilat.

Table of Contents

2 Scientific background 1
2.1 Energy balance equation 1
2.2 Eddy Covariance method 2
2.3 Bulk formulae 2
2.4 Controls on air-sea fluxes 3
3 Study region 5
4 Research objectives 8
5 Methods 9
5.1 Instruments 9
5.1.1 Eddy Covariance tower 9
5.1.2 High-frequency hydrographic data 9
5.2 EC Footprint and data quality 9
5.3 Post-processing 10
5.4 Gap-filling 11
5.5 Heat storage 13
5.6 Bulk formula 14
6 Results 15
6.1 Micrometeorology and water temperature 15
6.2 Energy balance equation components 17
6.2.1 Net radiation 17
6.2.2 Latent heat 18
6.2.3 Sensible heat 19
6.3 EC vs. bulk formula 19
6.4 Sea water residual- net surface heat exchange 20
6.5 Synoptic forced winter heat loss event 23
7 Discussion 26
7.1 Evaporation rates in the GoE: direct measurements vs. indirect estimates 26
7.2 Diurnal cycle and water temperature regulation 27
7.3 Energy balance closure and advection term estimation 28
7.4 Winter synoptic-scale forcing for high rates of heat loss 28
8 Conclusions 29
9 Appendix A 31
10 Appendix B 33

11 Appendix C: Evaluating how the travel distance of the winds over the sea effect heat exchange 36

12 Data availability statement 38

13 References 39

14 תקציר 43

2 Scientific background

Research of air-sea exchange of heat, gas, and momentum through surface fluxes, provides valuable insights into the physical and chemical processes of marine environments that sustain diverse ecosystems, such as coral reefs. Accurate quantification of exchange flux between the marine atmospheric boundary layer (MABL) and the surface of the ocean is valuable for climate models due to the large extent of the marine environment. Specifically, surface heat exchange is intertwined with the thermoregulation of the shallow water environment and basin scale thermo-haline dynamics.

The atmospheric boundary layer (ABL) is commonly described by the Monin-Obkhuv Similarity Theory (MOST). The theory describes the ABL dynamics in a non-dimensionalized form, outside neutral conditions as a function of the important non-dimensionalized parameter, Monin-Obkhuv height (Pal Arya, 1988). The MOST theory is the basis for key modeling methods and measurement instruments of processes in the ABL due to the complexity of turbulent processes. Both the bulk formulae approach (Sect. 1.3) and the Eddy Covariance (EC) direct measurement approach (Sect. 1.2) are formulated around MOST. The air-sea energy fluxes calculated by the bulk formulae or EC approach are two of the components of the energy balance equation (Sect. 1.1), latent and sensible heat.

2.1 Energy balance equation

The principle of energy conservation provides a comprehensive framework for thermoregulation in a marine environment and energy partitioning. It incorporates all of the heat fluxes involved in a marine environment from the surface of the ocean to the ocean bed, captured by the following equation:

$$(\mathrm{DSW} - \mathrm{USW}) + (\mathrm{DLW} - \mathrm{ULW}) = \mathrm{LE} + \mathrm{SH} + \mathrm{G} + \mathrm{Q_A}, \quad (1)$$

The left-hand side of Eq. (1) terms are the radiation components. These are the downwelling (DSW) and upwelling (USW) shortwave radiation which are related through the albedo term of the water, and downwelling (DLW) and upwelling (ULW) longwave radiation. The right-hand side of Eq. (1) includes the Latent heat flux (LE) and sensible heat flux (SH), both can be accurately measured. G refers to the change in heat storage in the water column. Net horizontal advection of heat in the water due to currents and tides is represented by $\mathrm{Q_A}$. Therefore, in areas where reverse estuarine circulation occurs and where fluvial discharge and rain contribution are negligible, air-water interaction is directly connected to the general circulation through $\mathrm{Q_A}$.

Ultimately aggregating the shortwave and longwave radiation into the net radiation (RN) which is interpreted as follows; positive values are net gain of energy to the water from longwave and shortwave radiation and negative values are net loss of energy from the water to the air:

$$RN = LE + SH + G + Q_A, \quad (2)$$

RN is measured easily with a net radiometer over the sea, while G and Q_A are difficult to measure due to the complexity of setting an entire water column mooring array.

2.2 Eddy Covariance method

The most accurate way to acquire the LE and SH fluxes (Eq. (2)) is by the EC method (or Eddy Correlation) which is the application of an Eddy Covariance measurement tower. EC method is based on simultaneously measuring the turbulent velocity and scalar quantity fluctuations (temperature/specific humidity are the scalar components measured for SH and LE respectively). The covariance of these components is prescribed as follows (Pal Arya, 1988):

$$LE_0 = 10^{-3} \cdot \rho \cdot L_v \cdot \overline{w'q'}, \quad (3)$$

$$SH_0 = \rho \cdot C_p \cdot \overline{w'T'}, \quad (4)$$

Where ρ is the air density (Kg m^{-3}), C_p is the specific heat capacity in constant pressure (J Kg^{-1} K^{-1}), L_v (J g^{-1}) is the latent heat of the vaporization of water, w' (m s^{-1}) is the vertical wind, q' (Kg Kg^{-1}) is the specific humidity, and, T' (°K) is the air temperature; the prime denotes turbulent fluctuations and the over-bars denotes the time mean. The resulting zero-order (prior to any corrections) fluxes of SH_0 and LE_0 are given in W m^{-2}.

In recent decades, the measurement of the energy exchange components in marine and lacustrine environments has undergone significant advancements, particularly by using EC towers that offer direct and accurate measurements of the turbulent fluxes of LE and SH between the water surface and the ABL (Fairall et al., 1996; Hamdani et al., 2018; Lensky et al., 2018; McGowan et al., 2019; Mor et al., 2018; Pérez et al., 2020; Rey-Sánchez et al., 2017; Tau et al., 2022). EC campaigns focused on air-sea exchange are rare and primarily ship cruise based (bound to the logistical constraints of cruises) therefore short, and non-stationary. So far, these campaigns measured low values of LE (mean LE of 70-90 W m^{-2}) (Fairall et al., 1996; Santini et al., 2020).

2.3 Bulk formulae

The LE and SH fluxes are commonly estimated by bulk formulae methods due to the relative difficulty of the EC method (costly, high demand of power supply, etc.).

The bulk formulae method is a widely adopted approach in estimating surface energy fluxes due to its reliance on easily obtainable variables, namely: sea surface temperature, air

temperature, and a 2D wind measurement at 10 meters. The bulk formulae method calculates the latent heat flux (W m^{-2}) by multiplying the wind speed (Ws), specific humidity difference between the water surface and the air (Δq), and a dimensionless vapor transfer coefficient (C_e) (Kondo, 1975):

$$LE = L_v \cdot \rho \cdot C_e \cdot Ws \cdot \Delta q, \quad (5)$$

$$SH = \rho \cdot C_p \cdot C_h \cdot Ws \cdot \Delta T, \quad (6)$$

Where ρ is the air density (Kg m^{-3}), L_v (J g^{-1}) is the latent heat of the vaporization of water, Ws is in m s^{-1}, and Δq is given in Kg Kg^{-1}. Eq. (6) describes the bulk formula calculation of sensible heat (W m^{-2}) includes the temperature difference between the sea surface and the air (ΔT), the heat capacity of air in constant pressure (C_p) (C_p is chosen accordingly to the units of temperature Kelvin or Celsius), and dimensionless heat transfer coefficient (C_h). This thesis focuses primarily on the LE due to its much higher typical intensity. This approach for estimating surface energy fluxes relies heavily on the parametrization of the vapor transfer coefficient, which involves several assumptions and empirical relations for calculating the Monin Obukhov length and the friction velocity (Fairall et al., 1996). Both can vary significantly in coastal regions according to the parametrization method (Bardal et al., 2018). While projects such as TOGA-COARE (Fairall et al., 1996) have aimed to reduce uncertainties in the vapor transfer coefficient, their findings are primarily applicable to the tropical open ocean, where an unstable MABL is persistent. However, in stable ABL conditions that are common in sea areas where flow originates from land, like the northern Red Sea, and coastal upwelling areas, large uncertainties remain in momentum and scalar flux estimation (Edson et al., 2007). Moreover, the comparison of EC measurements and bulk formulae showed larger inconsistency during transient synoptic systems (Santini et al., 2020). These shortcomings indicate that discrepancies between the EC method and bulk formulae may originate from the vapor transfer coefficient parametrization. Thus, to overcome these uncertainties a long-term comparison to direct measurements is needed. Apart from the effect on each air-sea flux, the uncertainties are propagated into the energy balance of the system and therefore there is no energy closure, and the energy balance closure problem is unresolved (Yu, 2018).

2.4 Controls on air-sea fluxes

Diurnal to seasonal cycle processes of local micrometeorological parameters (i.e. wind, humidity, cloud coverage, etc.) and their variation due to the synoptic scale forcing, can significantly affect the energy balance partitioning and thermoregulation of shallow marine environments. Synoptic scale forcing, which leads to changes in humidity, wind speed, and air

temperature can have a rapid impact on the water temperature and overall energy balance (Abir et al., 2022; Genin et al., 2020; MacKellar & McGowan, 2010; Papadopoulos et al., 2013). Abir et al. (2022) showed how the summer energy balance at the Gulf of Eilat (GoE) protects the shallow coral reef from heat-induced stress. The strong evaporative cooling supported by the extremely dry air mitigated high water temperature in the diurnal cycle and after marine heatwaves. These findings suggest that understanding how the energy balance of marine environments behaves on a diurnal to seasonal cycle with response to local and regional micrometeorological factors and irregular synoptic scale events that affect these cycles should be considered a research priority.

The knowledge gaps in air-sea exchange research include limited Eddy Covariance campaigns which hinder our comprehensive understanding of controls on latent and sensible heat fluxes in marine environments. The uncertainties in the bulk formulae method, especially in stable atmospheric conditions and coastal regions, challenge previous estimations of heat partitioning between the sea and the air. The lack of energy closure in the system emphasizes the need for better parametrization and measurement techniques to improve energy balance estimations. Challenges in accurately measuring heat storage and net horizontal advection of heat due to technical complexities, therefore, require accurate energy balance equation components measurement to indirectly estimate them. An accurate understanding of the response of the air-sea fluxes to synoptic circulation forcing and its effect on the ocean circulation dynamics. This thesis aims to decrease the knowledge gaps in air-sea fluxes research while focusing on the GoE as an ideal natural laboratory due to its accessibility, the abundance of measurements and research, and the negligible amount of precipitation and fluvial inputs.

3 Study region

The study was conducted over the north-western shore of the GoE, Israel (Fig. 1a,b), a narrow (<25 km), deep (maximal depth 1800 m) sea semi-enclosed by a hyper-arid desert. The GoE is connected to the Red Sea through the Straits of Tiran in the south. Local winds are channeled by the Arava rift valley, bringing (most of the time) dry terrestrial northeasterly wind (along gulf component) to the northern GoE (Fig. 1e). During winter, less common southerlies affect the region. These are channeled by the GoE basin, traveling a longer distance over the sea compared to the prevailing northerly winds (Afargan & Gildor, 2015).

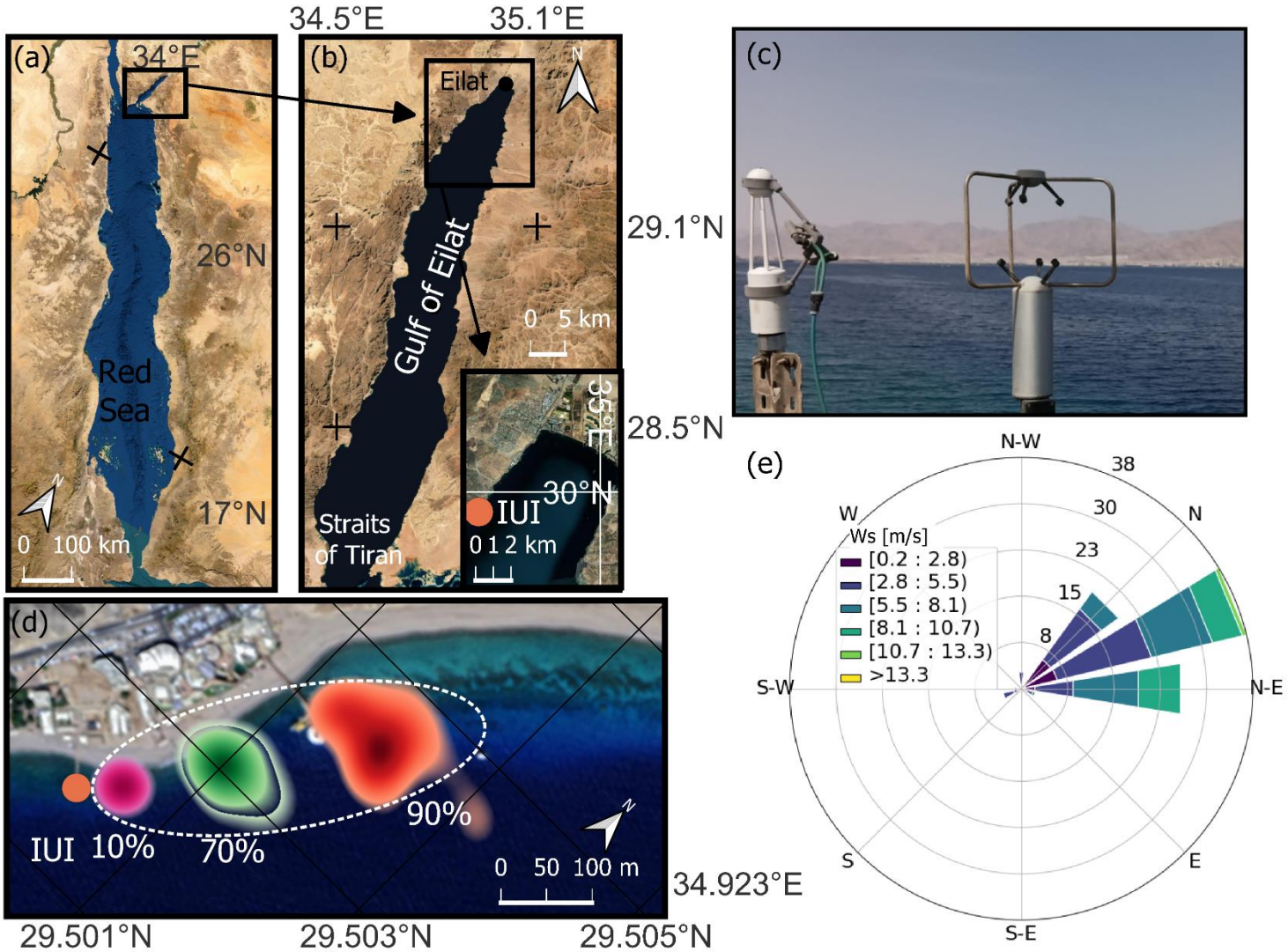

Figure 1: Location map and site description. Satellite images of (a) the Red Sea, (b) the Gulf of Eilat (Aqaba), and (b insert) the eddy covariance station location at the IUI. (c) The eddy covariance instruments, IRGA, and 3D wind anemometer. The footprint heatmap is also presented in (d); pink=10%, green=70%, and red=90% represent the percentile of the distances from which the data was collected by the EC, and the white dashed line is a schematic representation of the footprint area. (e) Wind rose diagram for the entire observation period; legend values are wind speed in ms^{-1} (September 2020- September 2022), and centric contours are percentile from the observations. Image ©: (a-b)- Data SIO, NOAA, U.S. Navy, NGA, GEBCO image © Landsat/ Copernicus, (b insert)- Data SIO, NOAA, U.S. Navy, NGA, GEBCO image © 2022 TerraMetrics, © 2022 CNES / Airbus, © 2022 Maxar Technologies, (d)- image ©2022 CNES/Airbus.

During summer (June, July, August hereafter JJA) the prevailing atmospheric synoptic circulation is a low-pressure system centered north-west of Israel (Persian Trough). During winter the common synoptic systems are Cyprus lows, Red Sea Trough (RST), and Siberian High. The Red Sea Trough (RST) is characterized by a region of surface low-pressure extending from the Red Sea to the coast of Turkey; it is common during transitional seasons and winter (Dayan et al., 2012). During winter (December, January, and February hereafter DJF) anti-cyclonic synoptic flow (intensified Arabian High an extension of the Siberian High) associated with surface high-pressure systems, can cause strong, cold, and dry westerly winds at the Red Sea. These anti-cyclonic flows result in extreme heat loss events through the latent and sensible heat fluxes (stronger than -400 W m^{-2}) (Menezes et al., 2019). In contrast, low-pressure systems are associated with lower heat loss values (values from -100 to -50 W m^{-2}), as these events are accompanied by warm and humid southerly winds (Papadopoulos et al., 2013). However, research on extreme heat loss events has been done on coarse satellite data (~0.5^{o}), therefore an accurate representation of the GoE is lacking due to its small dimensions and indirect flux estimation (conducted on the OAFlux and MERRA-2 dataset).

Short periods of EC measurements conducted at the GoE (Abir et al., 2022; Rey-Sánchez et al., 2017) during summer measured an evaporation rate of >10.3 mm day^{-1}. Thus, showing discrepancies between the evaporation rates estimated by bulk formulae during summer (~3 mm day^{-1}) and maximum evaporation during winter (11 mm day^{-1}). These bulk formulae explained the higher winter evaporation by the ABL instability due to warmer surface water than the overlying air (range of bulk formulae estimation: [1.6,3.65] m $year^{-1}$ (Assaf & Kessler, 1976; Ben-Sasson et al., 2009; Eshel & Heavens, 2007; Sofianos et al., 2002)). These findings highlighted the need for implementation of accurate and direct measurement methods of the turbulent fluxes, to better understand the complex energy balance dynamics in the GoE. Similar characteristics probably exist in other desert-enclosed basins, such as the Red Sea or the Arabian Gulf.

The general circulation model of the GoE which was originally proposed by Klinker et al. (1976), was characterized as reverse estuarine circulation and was the widely accepted model. The model postulated that buoyancy circulation driven by heat loss and evaporation is the primary driving force behind the GoE circulation. Biton & Gildor (2011b) proposed a seasonally varying model, where the maximal exchange flux between the northern Red Sea and the GoE occurs during the re-stratification season (April to August). It is, driven by density differences between the basins, while atmospheric fluxes counteract this exchange flow. They

attributed the observed warming of the surface primarily to the advection of warm water from the northern Red Sea, with a smaller contribution from surface heating.

Since the winter of 2011/2, the vertical winter basin overturning (vertical mixing) did not exceed a depth of ~500 meters until the winter of 2021/2 which exceeded 700 meters (Shaked & Genin, 2022).

The alongshore currents in the northwestern terminus shore where the EC was located typically flow from north to south in response to tides and winds (Berman et al., 2000, 2003). Daily shallow water temperature at the GoE varies from ~21.5 °C (minimum 20.5 °C) during winter to ~27.5 °C (maximum 30.5 °C) during summer (based on measurements from 2007 to 2021 conducted by Israel's National Monitoring Program (NMP)). The average annual open sea SST increased by an average rate of more than 0.5 °C decade^{-1} since 2004 (Shaked & Genin, 2022).

4 Research objectives

The research seeks to accurately quantify the diurnal to seasonal cycles of the air-sea heat exchange at the semi-enclosed sea of the GoE and to examine governing local and regional controls and the effect of these fluxes on the basin scale dynamics. The specific objectives are as follows:

1. Evaporation rates and associated micrometeorology: to investigate the seasonal and diurnal variation in heat exchange fluxes; to analyze the relationship between wind speed, vapor pressure difference, evaporation rates, and their diurnal and seasonal cycles.
2. Bulk formulae error: to determine the main cause of bulk formulae evaporation rate error in stable atmospheric conditions in the GoE.
3. Net energy exchange and heat budget: to evaluate the contribution of heat advection to the overall heat budget.
4. Wintertime atmospheric circulation impacts heat loss in the GoE: to investigate the synoptic scale forcing on the energy balance during extreme heat loss event, and the processes that lead to winter water column vertical mixing.

5 Methods

5.1 Instruments

5.1.1 Eddy Covariance tower

The eddy covariance system consisted of an open path CO2/H2O infrared gas analyzer (IRGA; model LI 7500, LI-COR, Inc., USA) coupled with a three-dimensional ultrasonic anemometer (R.M. YOUNG 81000), both recorded at 20 Hz using a CR1000X data logger. The station (Fig. 1c) was mounted on a ~7 m high mast above the mean sea surface, ~36 m offshore, positioned at the end of the wharf (29.510748°N, 34.917669°E) of the Interuniversity Institute for Marine Sciences (IUI). Solar and maritime radiation exchanges were measured by a CNR1/CNR4 net radiometer (Kipp & Zonen B.V., The Netherlands) mounted on the south side of the wharf of the IUI station extending ~1.5 m out from the wharf, and 1.5 m above the water surface. Air temperature and relative humidity were measured by HC2S3 probes (Campbell Scientific, USA). Water skin temperature was measured by an SI-4H1 infrared radiometer (Apogee Instruments, Inc.). Water temperature (measured at a water depth of ~1 m) at IUI and also relative humidity, air temperature, DSW, and wind measurements for gap-filling purposes were obtained through the NMP at the GoE (http://www.meteo-tech.co.il/eilat-yam/eilat_en.asp). The LI-COR 7500 open path gas analyzer and net radiometer were regularly washed to ensure the sensors were free of salt and dust.

5.1.2 High-frequency hydrographic data

An ocean mooring equipped with a Del Mar Oceanographic's WireWalker, hereinafter WireWalker was used. The WireWalker is purely mechanical and profiles continuously, with wave energy driving the buoyant profiler downward. On reaching the deepest user-specified sampling depth, it free-ascends along its suspension cable (aka profiling wire), nearly completely decoupled from mooring motion. The WireWalker was equipped with an RBRconcerto CTD. The RBRconcerto CTD was programmed to work in Directional mode: with fast sampling (8 Hz) in the ascending direction and a slow sampling rate (1 Hz) while descending. In this work, only upcast data was used. The RBRconcerto CTD measured the temperature, salinity, and velocity from 3 m down to 150 m between 10/11/2021 06:00:00 and 23/11/2021 12:14:55, 08/02/2022 6:22:35 - 03/03/2022 8:34:35, and 06/07/2022 8:00:00 and 27/07/2022 10:43:52.

5.2 EC Footprint and data quality

EC measurement footprints (Fig. 1d) were calculated using the EddyPro© program (LI-COR Biosciences, 2021). To minimize data "contamination" of the footprint a wind direction filter

was applied to exclude wind from land (excluded wind directions: 225°-360°). The water surface is not static due to water motion (currents, waves, tides), however, it can be regarded as a static surface, since the water motion velocity is two orders of magnitude smaller than wind velocity. Maximum tidal changes in the GoE are small and may offset the 90% footprint distance by only a few tens of meters, i.e., 622 to 700 m (~ 10%), and are therefore considered not to greatly affect energy flux measurements. In addition, low-quality data were excluded, using the Foken flag method (Foken et al., 2004) (data categorized as Foken flag=2 was excluded), and post-processing manual spike removal was conducted so that latent heat (LE) and sensible heat (SH) fluxes were restricted between -50 to 1100 W m^{-2} and ± 250 W m^{-2} respectively. The resulting percentage recovery of 30-minute mean flux data was 45%/46% (LE/SH) before gap-filling which is typical of the recovery rate of shoreline-mounted EC stations (Gutiérrez-Loza & Ocampo-Torres, 2016). During April- June 2022 the EC station recorded at a frequency of 4 Hz due to an error, the reader is referred to Fig. B1 in Appendix B for an analysis of the uncertainty in the fluxes due to this error, in which the mean difference for the latent and sensible heat is of 30 W m^{-2} and 3 W m^{-2} (respectively), between 4 and 20 Hz measurements.

5.3 Post-processing

This subsection describes the calculation of additional meteorological parameters relevant to the energy balance analysis, and the assumptions and methodologies of the calculation of the energy balance equations (Eq. (1)).

Half-hourly energy fluxes (Abir et al., 2023) were obtained using the EddyPro© program (LI-COR Biosciences, 2021). The program was run in Express mode which includes defaulted filters and corrections (LI-COR Biosciences, 2023) upon the zero-order fluxes in Eq. (3) and Eq. (4).

The contribution of rain (annual average precipitation from 1990-2020 is 23 mm (Israel Meteorological Service, 2023)) to the energy balance is negligible, as the study site is located in a hyper-arid desert. The heat exchange across the seabed is also considered to be negligible in this study due to its typical values being usually a minor contributor to the energy balance equation (Pivato et al., 2018; Shalev et al., 2013). Q_A is hard to measure in the GoE since geopolitical constraints prevent across-gulf measurements of currents and temperatures, and in this thesis is inferred as a residual from the surface energy fluxes (RN, LE, and SH) and the change in heat storage. When the change in heat storage measurement is not available, then sea

water residual will be reported (Q_{SWR}) which is the net surface exchange ($Q_{SWR} = RN - LE - SH$) (McGowan et al., 2010).

The vapor pressure difference between the water surface and the overlying air is given by:

$$\Delta e = \beta \cdot e_{sat}(T_w) - \frac{RH}{100} \cdot e_{sat}(T_a) = e_w - e_a, \quad (7)$$

where Tw and Ta are the water and air temperature, respectively, and are given in °C, $e_{sat}(T)$ in mbar is the saturation vapor pressure by the Magnus-Tetens formula, β is water activity set to be 0.98 which is a typical value for seawater (Sverdrup et al., 1942), RH is the relative humidity, e_w and e_a are the water and air vapor pressure in mbar (respectively), and Δe is the vapor pressure difference in mbar.

5.4 Gap-filling

Gaps (gaps duration ~6 h) in the relative humidity (RH), wind speed (W_s), water temperature (Tw), and air temperature (Ta), where data was missing due to the station undergoing quarterly maintenance. These gaps were filled first by replacing the missing data with the data from an adjacent sensor from the NMP. Following that, a bi-linear, periodic trended interpolation (Morin et al., 2014) was used for small gaps.

Due to the malfunction of the downward-facing pyrgeometers of the CNR1 (September 2020-April 2022), the ULW was calculated in W m^{-2} from the water temperature measurement according to the Stefan-Boltzmann law:

$$ULW = \varepsilon \cdot \sigma \cdot Tw^4, \quad (8)$$

Where ε is the emissivity ($\varepsilon = 0.985$), σ is the Stefan-Boltzmann constant ($\sigma = 5.6697 \times 10^{-8}$ W m^{-2} K^{-4}) and Tw is the water temperature in °K.

The DLW was calculated based on Bignami et al. (1995); cloud coverage effect on the calculation was determined to be negligible (Ben-Sasson et al., 2009):

$$DLW = \sigma \cdot Ta^4 \cdot (0.65 + 0.00535 \cdot e_a), \quad (9)$$

Equations (8) and (9) were used to gap fill during the period where the station measured in 4 Hz mode which interfered with the data collection of the CNR4, and general gap filling.

The USW was calculated as a fracture of the downwelling shortwave radiation (Paynes, 1972):

$$USW = 0.065 \cdot DSW, \quad (10)$$

The DSW was gap filled by taking the measurement from the adjacent NMP sensor and Eq. (10) was used to fill gaps in the USW. The difference between the calculated net radiation mean and the measured net radiation mean was 50 W m^{-2}, which is 20% out of the measured mean (during a month where there were no gaps in the net radiometer data).

To fill gaps in LE and SH an Artificial Neural Network (ANN) algorithm was utilized (Mahabbati et al., 2021). The 2-year data set was divided into training (80%) and test (20%) datasets where each fifth week in the original dataset was set aside for testing.

The algorithm was implemented with Python sklearn.neural_network MLPRegressor package when the hyperparameters (learning rate, hidden layer, and maximum iteration number are specified in Fig. 2, 3) were chosen by a grid search cross-validation algorithm. The evaluation of the ANN performance reis presented in Fig. 2, 3. The test dataset Root Mean Squared Error (RMSE) for the LE and SH ANN models was 92 and 25 W m^{-2}, respectively. The R^2 score for the test dataset for the LE and SH ANN models is 0.75 and 0.79, respectively.

Following the gap-filling procedure, the resulting percentage recovery of 30-minute mean flux data was >99%.

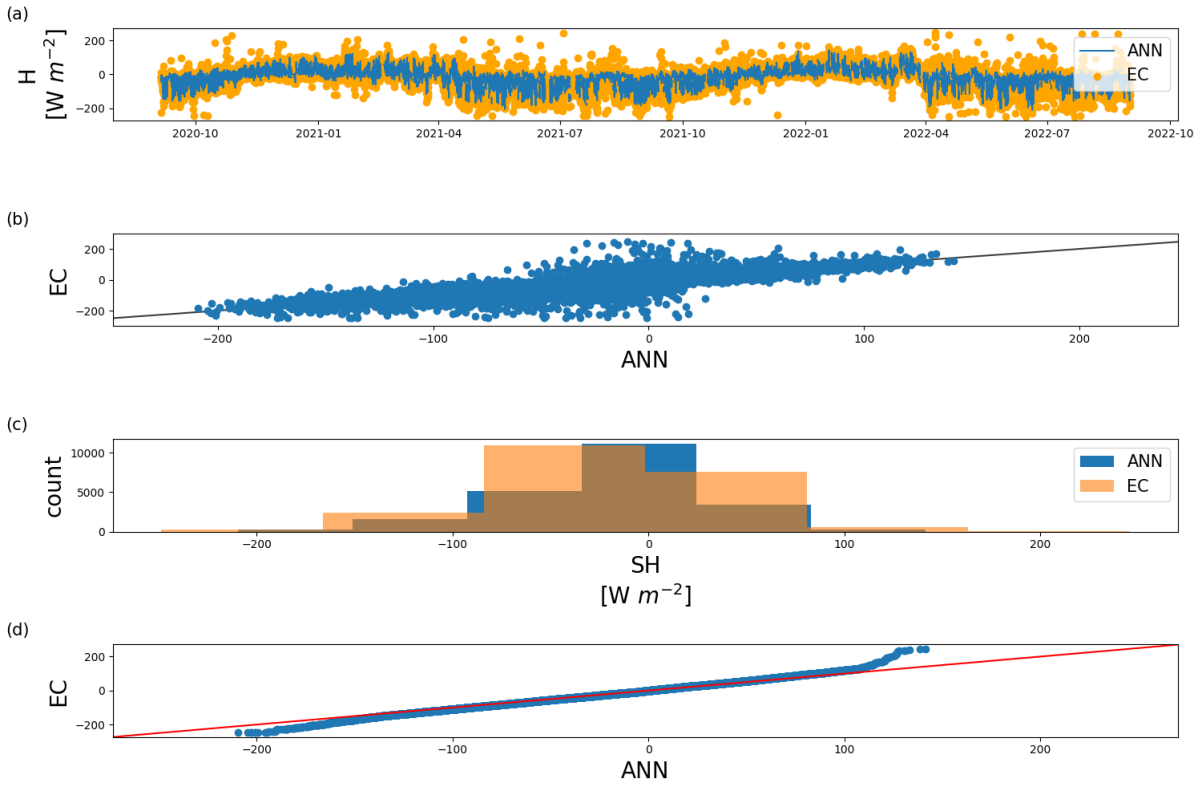

Figure 2: Comparison between the EC-measured sensible heat flux and the ANN gap-filling method, units are in W m^{-2}. (a) Time series comparison, (b) scatter splot comparison (black line is the 1:1 line), (c) histogram of EC measurements and ANN, (d) q-q plot (red line is the 1:1 line). ANN hyperparameters: hidden_layer_sizes= (400,500), max iter=500, learning_rate_init=0.001).

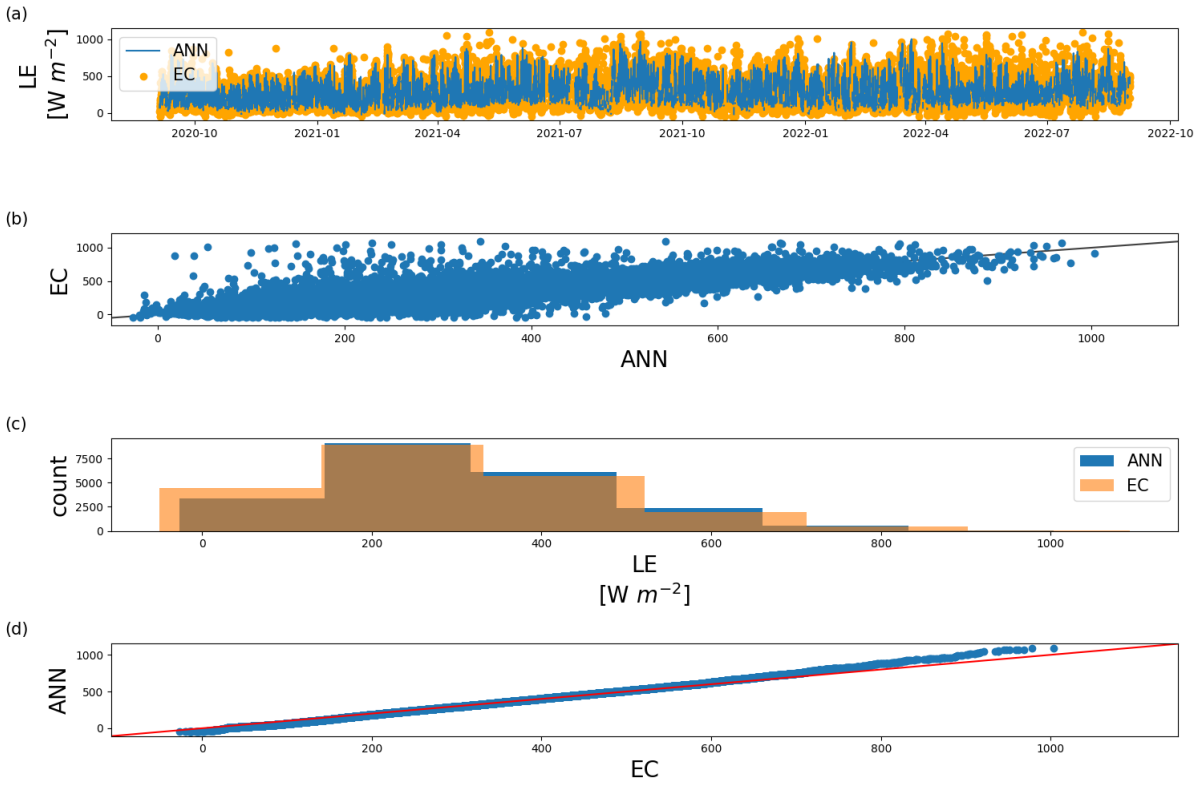

Figure 3: Comparison between the EC-measured latent heat flux and the ANN gap-filling method, units are in W m^{-2}. (a) Time series comparison, (b) scatter plot comparison (black line is the 1:1 line), (c) histogram of EC measurements and ANN, (d) q-q plot (red line is the 1:1 line). ANN hyperparameters: hidden_layer_sizes= (400,400), max iter=400, learning_rate_init=0.001).

5.5 Heat storage

The profiles collected by the RBRconcerto CTD (described in Sect. 4.1.2), where de-spiked (threshold=4.0, windowLength=11), bin averaged (bunBy=depth, boundary=[0.5,145]) using the pyrsktools python library. The resulting profiles are from 0.5-145 meters at 1-meter intervals. For the calculation of the heat storage, the temperature profile was smoothed using python scipy.signal library savgol_filter function (window_length=5, polyorder=3) and then interpolated to fill missing data points. The total heat of the water column of each preprocessed CTD profile was then computed according to the:

$$Hg = \rho \cdot C_p \cdot \overline{T} \cdot \Delta Z, \quad (11)$$

Where Hg is the total heat of the profile water column in J m^{-2}, ρ is the seawater density, and C_p is the heat capacity at a constant pressure of seawater ($\rho \cdot C_p = 4.1 \cdot 10^6$ J m^{-3} °C^{-1}) (Each profile was assigned the mean timestamp of the profile), $\overline{T}$ is the mean temperature of each 1-meter water layer in the profile and ΔZ is the 1-meter water layer thickness. The total heat was downsampled to a 1-hour frequency with a weighted average algorithm (mean time between profiles is ~22 minutes) and then underwent a rolling averaged procedure with a 2-day centered

window to eliminate internal wave oscillation in the data. The total heat was then smoothed with a savgol filter (window_length=15, polyorder=3). Lastly, the change in heat storage was calculated:

$$G = \frac{\Delta Hg}{\Delta t}, \quad (12)$$

Where G is the change in heat storage in W m^{-2}, ΔHg is the change in total heat between adjacent profiles, and the Δt in second is the time between them (1 hour).

5.6 Bulk formula

The bulk formula (Eq. (5, 6)) used to compare air-sea fluxes at the GoE is the COARE3.6 algorithm (Fairall et al., 1996). The NMP measurements were used as input data for the algorithm, hence, this analysis is comparable to previous works that utilized this data and for future reference. The Bulk Richardson number (Ri_B) which is used by the bulk formula to indirectly parameterize the stability parameter (ζ) is given by:

$$Ri_B = \left(\frac{g}{Ta+273.16}\right)\left[(\Theta - \Theta_0 - f(Ta, \Delta q)) \cdot \frac{z}{(Ws)^2}\right], \quad (13)$$

Where g (m s^{-2}) is the gravity acceleration, Θ and Θ_0 (°K) are the potential temperature calculated from Ta and Tw respectively, z (m) is the measurement height of the wind speed, Ws is the wind speed (m s^{-1}), and $f(Ta, \Delta q)$ is a correction term for the potential temperature difference due to the air lapse rate and cool skin effect (Δq is the specific humidity difference between the water surface and the air in g Kg^{-1}). To compare the bulk formula vapor transfer coefficient (C_e) to the EC measurements, C_e was calculated from the EC LE flux:

$$C_e = \frac{LE}{Ws \cdot \Delta q \cdot \rho_a \cdot L_v}, \quad (14)$$

Where ρ_a (Kg m^{-3}) is the air density and L_v (J g^{-1}) is the latent heat of the vaporization of water both calculated following Fairall et al. (1996).

6 Results

6.1 Micrometeorology and water temperature

The 2-year (September 2020-September 2022) measured local micrometeorology and their mean diurnal cycles per season are presented in Fig. 4 and Fig. 5, respectively.

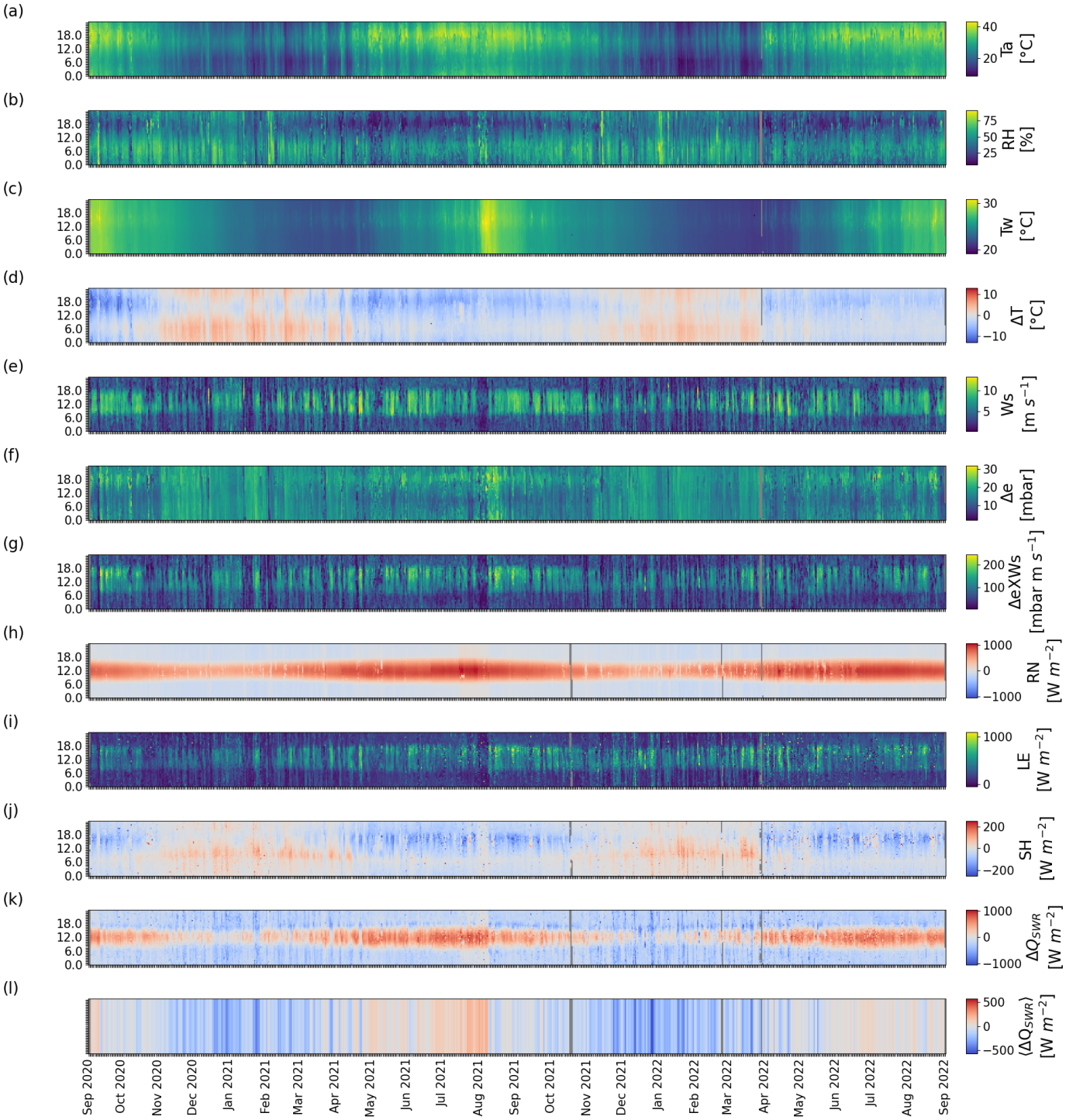

Figure 4: Diurnal (LT) and seasonal variations (y and x axes, accordingly) of the following parameters, measured during September 2020-September 2022: (a) Air temperature (Ta), (b) relative humidity (RH), (c) water temperature (Tw), (d) water-air temperature difference (ΔT), (e) wind speed (Ws), (f) vapor pressure difference (Δe), (g) Δe × Ws, (h) net radiation (RN), (i) latent heat flux (LE), (j) sensible heat flux (SH), (k) sea-water residual (Q_{SWR}), (l) daily sea water residual change ($\langle \Delta Q_{SWR} \rangle$).

The mean air temperature and relative humidity during the observation period were 25.9 °C and 42% (respectively). The air temperature varied between the winter seasonal mean value of 18.7 °C to the summer seasonal mean value of 32.1 °C. Relative humidity seasonal mean varied between a maximum value of 47 % during autumn (September, October, November hereafter SON) and winter (DJF) to a minimum value of 39 % during summer (JJA) and spring (March, April, May hereafter MAM) (Appendix A). The water temperature mean value was measured to be 24.7 °C, Tw was characterized by a low mean water temperature value of ~23 °C during winter and spring which then shifts to summer and autumn with higher mean values of ~26 °C. Consequently, the water at the GoE is warmer than the overlying air from November to March (Fig. 5f and Fig. B2 in Appendix B). The northeasterly (mean direction 23º) dominating winds have a mean seasonal wind speed of ~4.9 m s^{-1} observed through spring, summer, and autumn. The wind speed reaches the minimum value of 4.1 m s^{-1} during the winter (minimum out of the mean value per season). The seasonal mean diurnal cycle of wind speed (Fig. 5b and Fig. B2 in Appendix B) can be differentiated into two common cycles: Double peak and the bell-shaped curve. Both types, start to increase from the lower nighttime values, at ~06:00 LT reaching the first daily maximum of >6 m s^{-1} at ~10:30 LT, eventually, at ~15:00 LT, the wind speed decreases to <~5 m s^{-1} in winter, and at 17:00-17:30 LT during the rest of the year. The diurnal variations of Δe (Eq. (7), Fig. 5d) were characterized by daily mean minimum values occurring at ~09:00 LT (14 mbar) and the daily mean maximum values at ~18:30 LT (18 mbar). Additionally, from April-October the mean daily variations of Δe, are significantly more pronounced, concurrently with the water-air temperature difference (ΔT) and the RH daily variations. In winter the highest value of seasonal mean Δe is obtained (17.3 mbar) due to the positive ΔT (Fig. 5f) however, during the summer higher mean maximum daily values (26.3 mbar) are obtained due to the strong diurnal variations.

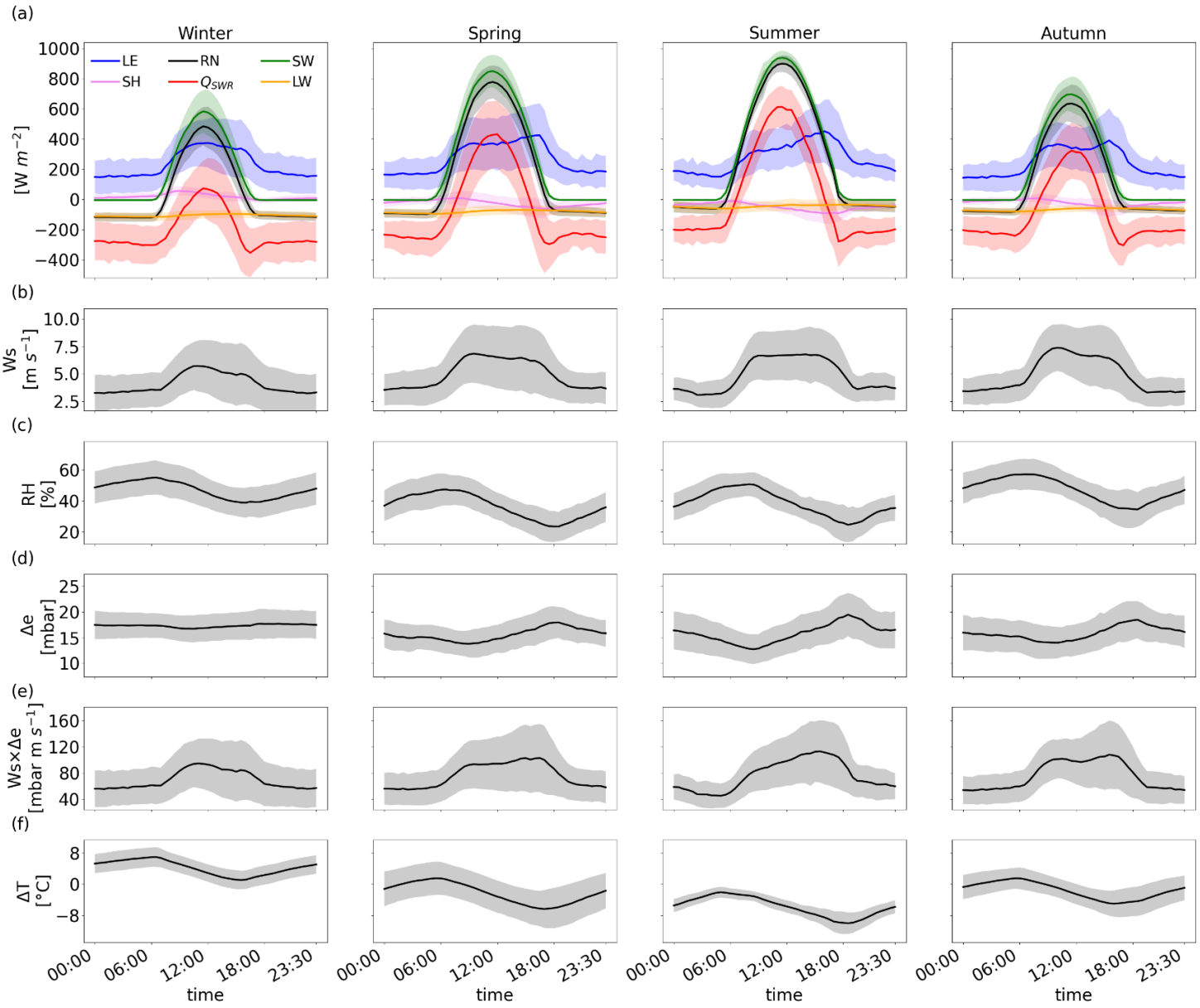

Figure 5: Seasonal mean diurnal (LT) cycle of micrometeorological and flux variables (Winter=December-January-February=DJF, Spring=March-April-May=MAM, Summer=June-July-August=JJA, Autumn=September-October-November=SON), and in the shaded area the +/- 1 SD span. (a) Energy fluxes, (b) wind speed (Ws), (c) relative humidity (RH), (d) vapor pressure difference (Δe), (e) Ws × Δe, (f) water-air temperature difference (ΔT).

6.2 Energy balance equation components

The 2-year (September 2020-September 2022) measured surface fluxes and their mean diurnal cycles per season are presented in Fig. 4 and Fig. 5, respectively.

6.2.1 Net radiation

The observation period mean RN value was 157 W m^{-2}, where positive values represent flux of energy from the atmosphere into the water surface. Net radiation mean diurnal cycle was of the characteristic bell-shaped and seasonal mean values varied between 55 W m^{-2} in winter to 252 W m^{-2} during summer (Fig. 5a). Nighttime net radiation values were negative, with

stronger ULW than the DSW (Fig. 5a), and with positive RN values during the daytime. The daily mean maximum temperature of Tw lags behind the mean daily maximum RN by 2.5 h, while the daily mean maximum Ta lags by 5.5 h (Fig. B2 in Appendix B).

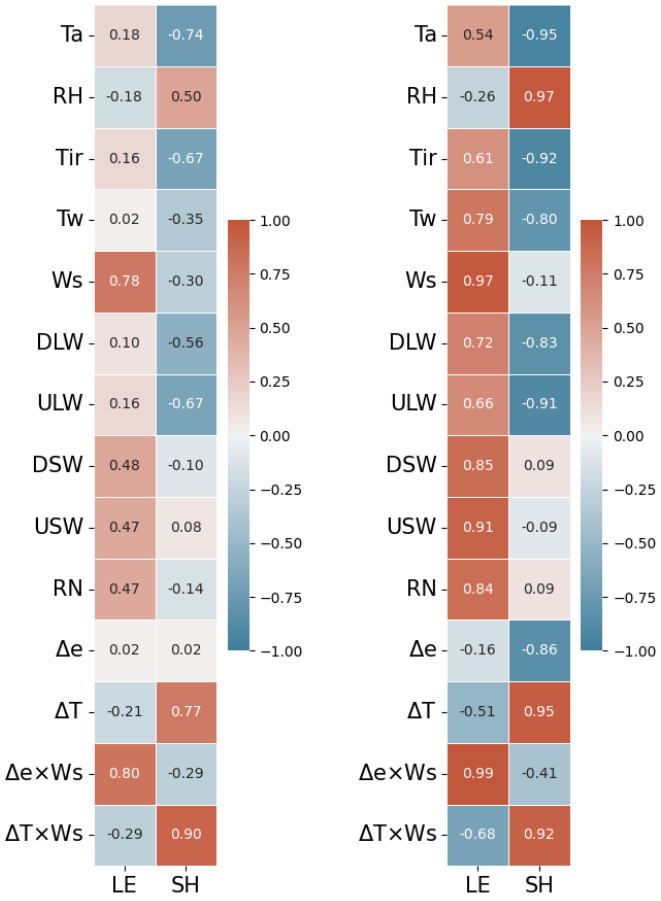

Figure 6: 30-minute data (left) and daily mean data (right) Pearson's correlation matrix of the sensible and latent heat fluxes with micrometeorological and radiation flux variables.

6.2.2 Latent heat

The mean LE flux of evaporation during the observation period was 255 W m^{-2} (3.22 m $year^{-1}$ of evaporation). Latent heat flux seasonal mean varied between the minimum values during winter (232 W m^{-2}) to the maximum during summer (276 W m^{-2}). As described in Sect. 5.1 for the Ws mean diurnal cycle, the LE flux mean diurnal cycle is categorized into two cycles; double peak and bell-shaped curve, where from mid-spring (April/May) to mid-autumn (September/October) there was a clear double peak in the diurnal LE cycle. The first peak coincides with the daily maximum wind speed (~10:00 LT) whereas, the second peak which was the absolute daily maximum (mean max value: 462 W m^{-2}) coincides with the product of the Ws and the Δe (Fig. 5e) at 15:30 LT. The product of the Ws and the Δe as prescribed by the bulk formulae approach has the highest correlation to the LE flux (0.99, Fig. 6 right). However, at the GoE the high correlation originated mostly from the correlation to the wind

speed profile of 0.97 (Fig. 5 right). The high correlation was visible in the temporal variations in both diurnal and seasonal plots (Fig. 5,6).

6.2.3 Sensible heat

The SH flux mean value through the observation period was -20 W m^{-2}. Concurring with the seasonal air-sea temperature difference cycle, the SH flux on average transfers heat from the water to the atmosphere during winter (winter mean values ~ 19 W m^{-2}), and continues to September and May (Fig. 5a and Fig. B2 in Appendix B). Spring to autumn mean seasonal value of SH flux ~-32 W m^{-2} corresponds to the relatively cool sea surface in a hot desert surrounding. Similar to the LE flux, the SH flux as well is highly correlated to the product of the Ws and a gradient; air–sea temperature difference (Pearson r=0.92, Fig. 6 right).

6.3 EC vs. bulk formula

Figure 7 presents the bulk formula calculation with the COARE3.6 algorithm of ABL meteorology parameters and the latent and sensible heat fluxes throughout the 2-year observation period compared to the EC-obtained variables.

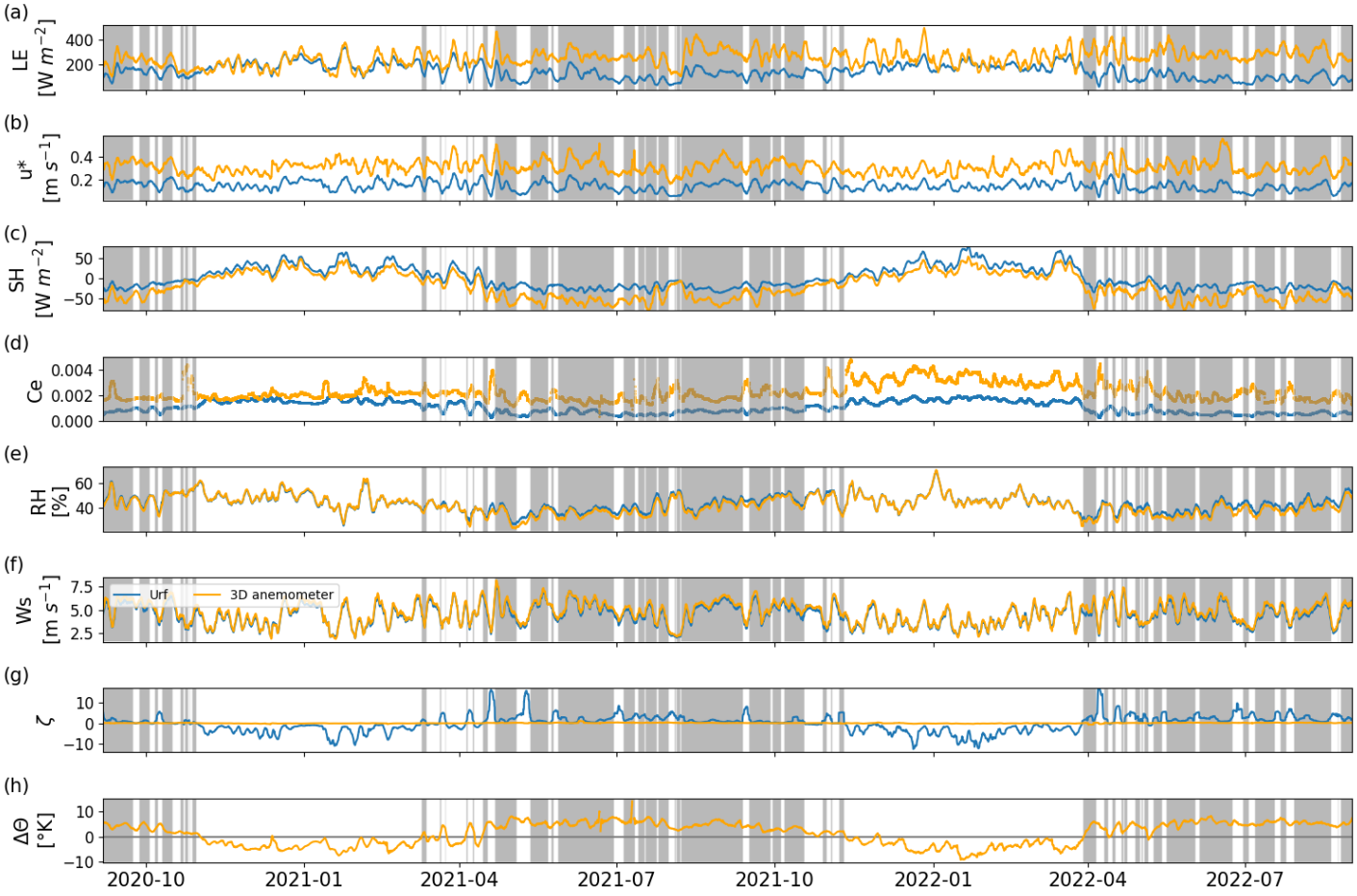

Figure 7: Comparison between the 3-day (LT) rolling average EC-measured sensible and latent heat fluxes and meteorological parameters (orange) and the bulk formula calculation using TOGA-COARE 3.6 algorithm (blue) computed with the NMP micrometeorological data. Shaded in gray are instances where the TOGA-COARE 3.6 algorithm bulk Richardson number is within the range of 0-0.2 indicating stable

conditions. The wind speed panel compares the measurements of the 3D sonic anemometer and the interpolated referenced height (7 m) of the TOGA-COARE 3.6 algorithm. (a) Latent heat (LE), (b) friction velocity (u^*), (c) sensible heat (SH), (d) vapor transfer coefficient (reversed calculated from the EC measurements Eq. (14)), (e) relative humidity (RH), (f) wind speed (Ws), (g) stability (ζ), (h) air and water potential temperature difference (Δθ). Key variations between the EC method and the bulk formula are higher evaporation rates measured with the EC system during stable conditions, consistent higher friction velocity measured with the 3D sonic anemometer, and low variation within the stability parameter calculated with the EC system.

The bulk formula for LE and SH at the GoE under-estimate (Table 1): During winter bulk formula mean (Fig. 7a,c respectively) values were the closest to the higher EC values. In Spring the difference between the two methods increased, reaching a maximum during summer. The annual maximum of the seasonal mean of the EC measurements was during summer whereas the bulk formula's was during winter.

	Winter		Spring		Summer		Autumn		Annual mean	
	LE	SH	LE	SH	LE	SH	LE	SH	LE	SH
EC (W m^{-2})	232	19	271	-25	276	-49	242	-22	255	-20
Bulk formula (W m^{-2})	199	34	144	-3	98	-22	146	-6	147	0.4

Table 1: EC and bulk formula seasonal and annual mean LE and SH fluxes comparison.

The measured 3D anemometer mean friction velocity (0.31 m s^{-1}) was ~2 times larger (Fig. 7b) than the bulk formula estimation from the 2D wind measurement (0.14 m s^{-1}). The ABL stability parameter (ζ) (Fig. 7g) showed a pronounced seasonal variation reaching its minimum value during the winter of ~(-12) and maximum value during the summer of ~17 with an overall mean value of -0.04. While ζ calculated by the EC system had a much less pronounced variation between the minimum and maximum values [-0.75,1.11], with a mean value of 0.06. The mean annual derived vapor transfer coefficient, C_e, from the EC LE is 0.00229 (Eq. (14)) whereas the bulk formula C_e is 0.00108 (Fig. 7d). However, the bulk formula seasonal means of C_e varied between two orders of magnitude while the EC-derived C_e varied in the scale of one order of a magnitude (seasonal mean range of bulk formula C_e: [0.00064, 0.00165] and EC: [0.00186, 0.00276]). The difference between the daily mean values of the SH flux calculated by the bulk formula and the EC approach is 20 W m^{-2}.

6.4 Sea water residual- net surface heat exchange

The seawater residual is calculated as the sum of the measured surface fluxes LE and SH, and RN, (i.e. net surface fluxes) it is presented in Fig. 4, and as a diurnal mean per season in Fig. 5. It is interpreted as heat gain (positive values) or loss (negative values) of the sea surface from/to (respectively) the air.

Q_{SWR} mean observation period value was -79 W m^{-2}, which lead to a net cooling of the surface water through the surface fluxes. Apart from summer, the seawater residual was negative,

reaching a minimum seasonal mean value of -195 W m^{-2} during winter and a maximum seasonal mean value of 27 W m^{-2} in summer. The mean diurnal cycle of the seawater residual was positive through ~08:00-15:00 LT, then in the afternoon, it was negative for the entire night and early morning. The change from the positive values of seawater residual to negative values in the afternoon coincides with the maximum of the mean daily cycle of the water temperature (Fig. 5 and Fig. B2 in Appendix B).

Figure 8 presents the available measured heat transfer components of the surface and water column heat exchange during three campaigns and also the advection flux as a residual form of the energy balance equation (Eq. (2)). Examining data from three campaigns for calculating GoE heat storage in the top 145 m of surface water showed that in the three campaigns, the deficit required to close the energy heat balance was 73, 88, and 175 W m^{-2} during winter, summer, and autumn respectively. During the winter campaign, there was a net cooling of the upper mixed layer, 0-145 m, (water column temperature and salinity ranged between 21.4-22.1 °C and 40.34-40.85 PSU, respectively). The net cooling is equivalent to -83 W m^{-2} in G. During summer there was net heating of the strongly stratified water (water column temperature and salinity ranged between 21.4-28.0 °C and 40.45-40.78 PSU, respectively), which was equivalent to a 95 W m^{-2} in G. During both campaigns, G did not equal Q_{SWR}. During autumn G of the mixed top water column was negligible (5 W m^{-2}) and the largest deficit in the heat balance closure exists due to the strong surface cooling (Q_{SWR}=-90 W m^{-2}).

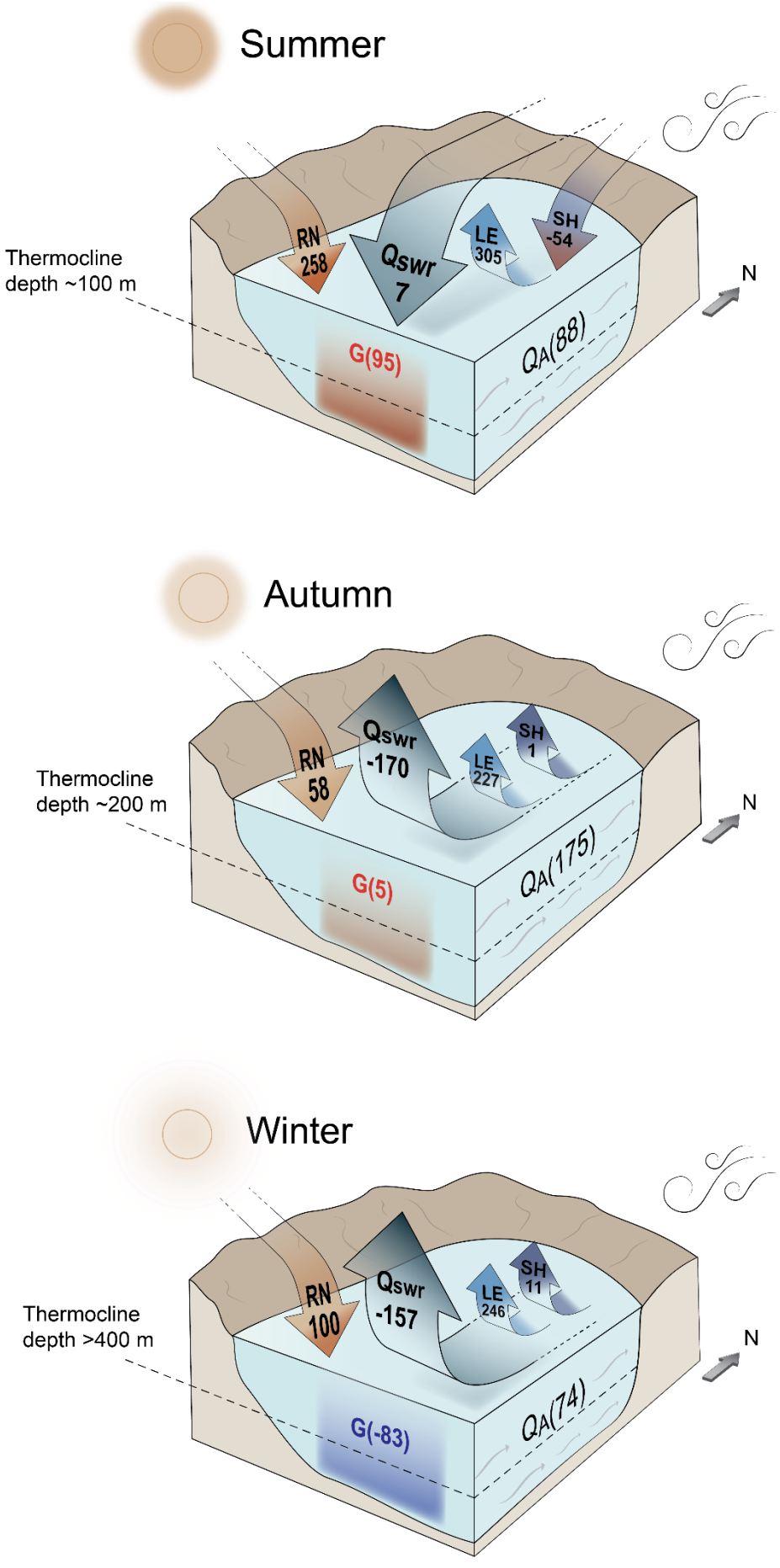
Summer
Thermocline
depth ~100 m
RN
258
Qswr
7
LE
305
SH
-54
N
G(95)
QA(88)
Autumn
Thermocline
depth ~200 m
RN
58
Qswr
-170
LE
227
SH
1
N
G(5)
QA(175)
Winter
Thermocline
depth >400 m
RN
100
Qswr
-157
LE
246
SH
11
N
G(-83)
QA(74)

Figure 8: Schematic representation of the mean energy partitioning at the GoE during the three campaigns when water temperature profiles are available (values are given W m^{-2}).

6.5 Synoptic forced winter heat loss event

Irregular synoptic scale forcing events were examined as drives to intensive heat loss from the water surface to the atmosphere. In the course of 3 days (25-27 December 2021) intensification of wind speed, and cooler and dry air mass forced high rates of heat loss from the sea surface to the atmosphere by LE and SH.

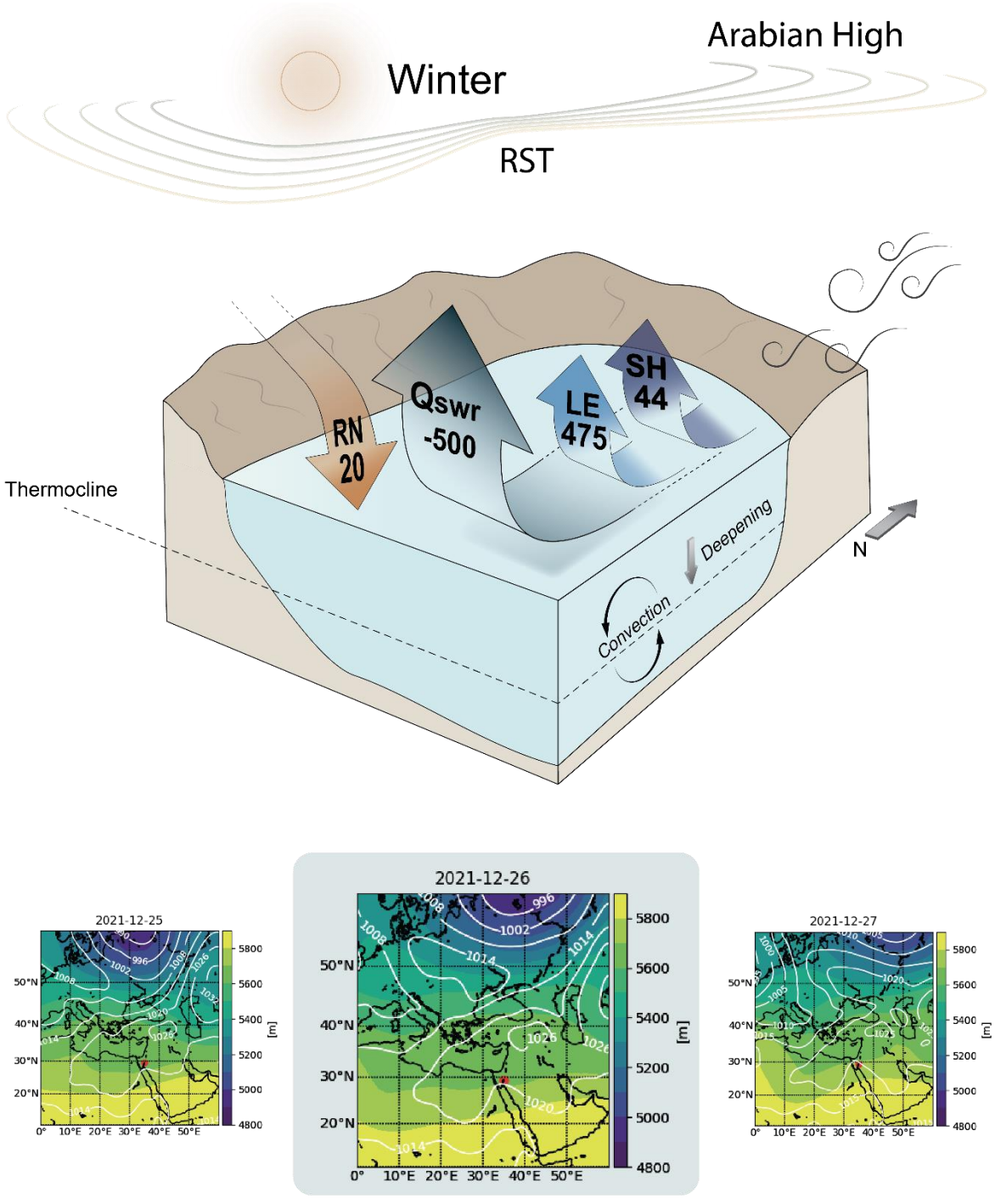

Figure 9: Surface heat loss case study synoptic maps (bottom) and schematic representation of the mean energy partitioning during the event (top). (Bottom) Average daily ERA5 reanalysis variables synoptic maps, sea level pressure (hPa) plotted in white in contour (Hersbach et al., 2023b), and the 500hPa geopotential height (m) plotted in shaded colors (Hersbach et al., 2023a). The event occurred between 25-27.12.2021 (the shaded map is the peak of the event) and involved the intensification of the Arabian High and the Red Sea Trough. (Top) Surface energy fluxes are given in W m^{-2}. The large heat loss is affecting the deepening of the thermocline and the winter annual vertical water column mixing.

Figure 9, presents the formation and decay of the RST (Alpert et al., 2004) surface-level synoptic state and intensification of the Arabian High, along side the mean energy partition of the large surface-water heat loss event. The described synoptic pattern caused an increase in daily mean wind speeds, from 3.8 to 5.9 m s^{-1} (Fig. 10a) relative to the season mean (DJF 2021-2). This mean increase manifested also in an increase of the minimum and maximum daily wind speed values at the GoE for the 3 days. Surface wind direction at the GoE was northeasterly (23º from the north), with an intensification of the westward component of the wind between 800 hPa to 500 hPa (Fig. B3 in appendix B) in the region. Additionally, during the event colder air masses in comparison to the sea temperature, were present in the GoE (the ΔT during the event was 1.5 °C larger than the season mean). The increase in Ws and ΔT forced large heat loss from the surface water of the GoE (Fig. 10i), -270 W m^{-2} stronger than the DJF mean which is 1.7 standard deviation (SD) of the season mean. The largest mean daily heat loss occurred on 26 December (mean daily value Q_{SWR}=-560 W m^{-2}) coinciding with the peak of the Ws during the event (8.9 m s^{-1}). The surface heat loss is a result of strong fluxes of LE and SH (Fig. 8f,g, respectively), which increased from 247 to 475 W m^{-2} (2 SD increase from the season mean) and 19 to 44 W m^{-2} (1.25 SD increase from the season mean), respectively. Unlike this event where the high Ws and mean values of RH and lower Ta (Fig. 10b,c respectively) resulted in large heat loss from the surface of the GoE, on 9 January 2022 (shaded yellow area in Fig. 10k) even higher mean daily wind speed (7.2 m s^{-1}) were measured. However, the mean LE flux measured only 314 W m^{-2}, and SH decreased to 2 W m^{-2}. Contrary to the portrayed heat loss event, on 9 January; warmer and more humid southerly winds persisted (184º). These air mass characteristics resulted in a decrease in Δe and ΔT ($\Delta e = 8.5$ mbar, ~9 mbar less than the season and the event mean value, $\Delta T = 0.8$ °C), which did not allow high rates of heat loss in comparison to the seasonal mean. Overall during the winter season of 2021/2, there were 7 days where the mean daily Q_{SWR} was stronger than -400 W m^{-2} in comparison to the previous winter of 2020/1 where only 2 days were recorded (mean winter Q_{SWR}= -195 W m^{-2}) . The synoptic pattern of 5 out of 7 of the days in winter 2021/2 was classified as either RST or high to the east (Arabian High) (see Alpert et al. (2004) for the classification method). Out of the 7 days, 2 events that prolonged a single day can be identified;

the first is a 2-day event and the latter is the prescribed 3-day event, thus large heat loss occurred mostly through events rougher than sporadic heat loss days.

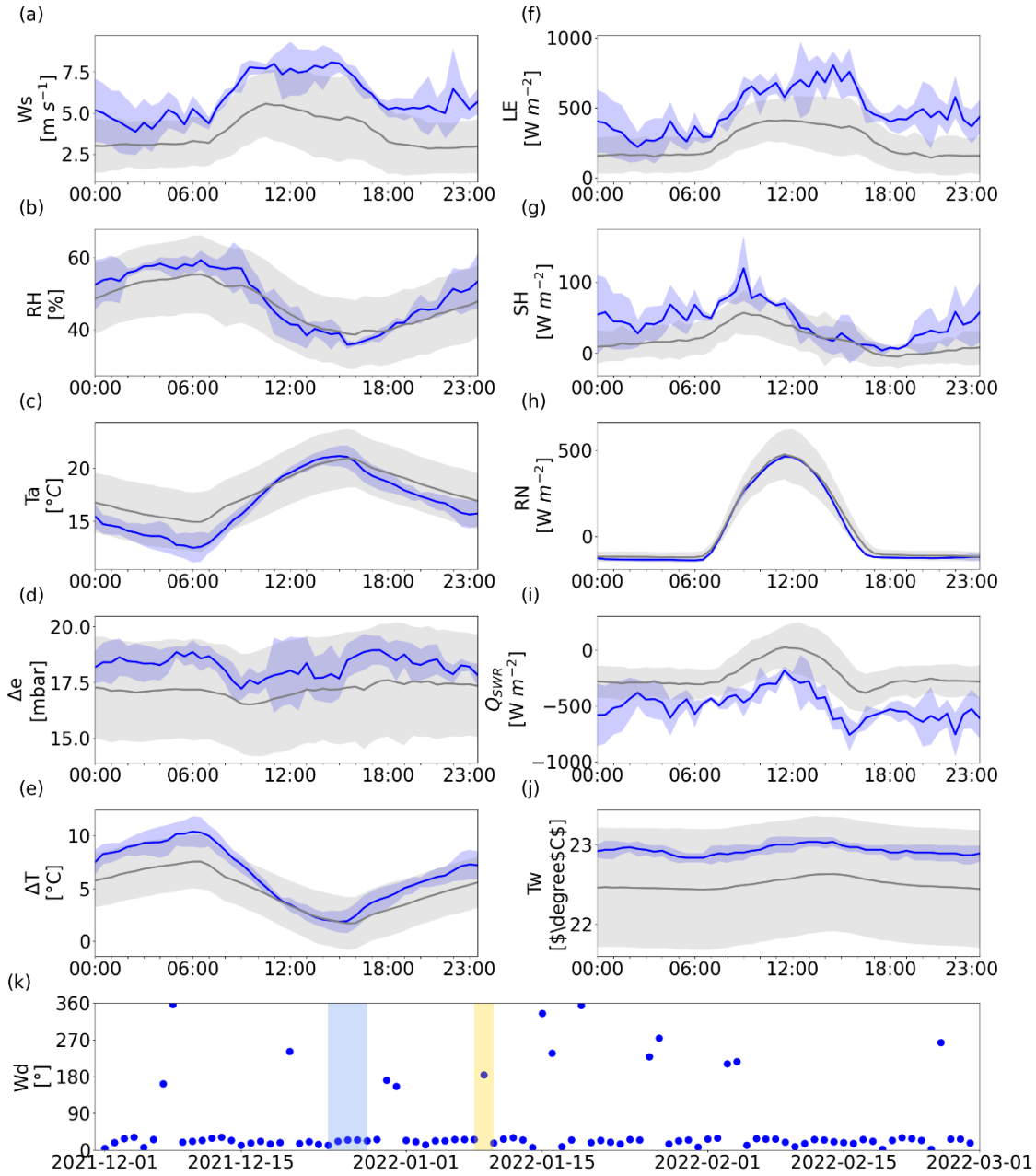

Figure 10: Extreme surface heat loss case study mean diurnal cycle (LT) during the event (blue) and the reference DJF 2021 period (gray) and in the shaded area the +/- 1 SD span. (a) Wind speed (Ws), (b) relative humidity (RH), (c) air temperature (Ta), (d) vapor pressure difference (Δe), (e) water-air temperature difference (ΔT), (f) latent heat flux (LE), (g) sensible heat flux (SH), (h) net radiation (RN), (i) water temperature (Tw), and (k) DJF mean daily wind direction, the blue shaded area marks the heat loss event (25-28 December 2021), and the yellow shaded area is the comparison event (9 January 2022) where the wind is sea originated; therefore, high air temperature and relative humidity prevent high rates of heat loss.

7 Discussion

Accurate quantification of heat and gas exchange between semi-enclosed seas and the atmosphere is essential for understanding the exchange of mass, momentum, and energy within the water column. The GoE, a semi-enclosed sea located in a desert region, is a perfect natural laboratory for studying air-sea interactions in marine environments where stable atmospheric boundary layer persists.

7.1 Evaporation rates in the GoE: direct measurements vs. indirect estimates

The annual mean evaporation rate of 3.22 m $year^{-1}$, presented here, is based on direct measurements and is approximately two times larger than earlier estimations based on indirect bulk formulae (Ben-Sasson et al., 2009). Our findings support the product of Ws and Δe as the main forcing mechanism for evaporation in the GoE, in agreement with Lensky et al. (2018) and Tau et al. (2022), with high correlations observed in both diurnal and seasonal time scales. However, in the extremely arid environment of the GoE where Δe is always positive and has high values, evaporation is mostly governed by the Ws (correlation of LE to Ws is 0.97, and to Δe × Ws is 0.98). Accordingly, although the mean Δe is higher in winter and the water surface temperature is higher than the overlying air temperature, thus promoting thermal convection. Evaporation is higher in summer due to the high wind speed that is sustained longer in the day and the coincidence with the high Δe during the afternoon. Ben-Sasson et al. (2009) estimated higher evaporation during winter, based on the bulk formulae approach, which overestimates the role of vertical thermal stability of the air (warmer water underneath the colder air); thus, they predicted that in winter, the free convection due to atmospheric instability led to increased evaporation rates.

The bulk formula estimation of the LE and SH fluxes reproduced similar seasonal trends and values as Ben-Sasson et al. (2009). The comparison to our EC measurements indicated that the bulk formulae are not appropriate for complex desert semi-enclosed seas. Specifically the parametrization of the ABL stability and the calculation of the friction velocity through their relation to the bulk Richardson number; indicated by the large deviation of the stability parameter and the lower friction velocity of the bulk formula in comparison to the EC values. These findings are consistent with the observations of Bardal et al. (2018) regarding the sensitivity of boundary layer stability to parametrization methods in coastal regions. When stable ABL is calculated using the bulk formula, a lower water vapor transfer coefficient is assigned, resulting in lower evaporation rates outside winter. These lower bulk formula

evaporation rates occur despite $\Delta e \times Ws$ being higher outside winter and therefore also the measured EC evaporation flux.

The complex nature of the sharp gradients between the arid landscape and sea and the proximity to the mountainous shore presents a challenge for the bulk formulae; it was originally calibrated for the open tropical ocean where unstable MABL conditions persist and rely on empirical relations. To address this issue, a similar effort to the TOGA-COARE campaign (Fairall et al., 1996) is required to refine the bulk formulae parameterization in this intricate environment. The efforts need to focus on the relationship between the easily computed bulk Richardson number and atmospheric stability and friction velocity. Until such efforts are made, it is recommended that the direct method of the EC approach be used, as it is the only method with sufficient accuracy for evaporation rate estimation in these settings and probably in similar regions such as the Persian Gulf and where coastal upwelling and land originated winds determine a stable ABL over the sea. It is also important to examine the spatial variability of the EC measurements in this environment where the wind is carried from land to sea. Specifically, to accurately measure the air-sea fluxes along the increasing distance from the shore along the GoE and the Red Sea (the reader is referred to Appendix C for analysis of the wintertime LE and SH fluxes variation with land/sea originated winds representing short and long travel time over the sea).

The SH flux is small compared to radiation and LE fluxes (-20 W m^{-2}) transferring overall heat from the air to the sea according to the air-sea temperature difference. The bulk formula like in the case of LE is underestimating the SH flux.

7.2 Diurnal cycle and water temperature regulation

The diurnal cycle of heat fluxes and micrometeorology shows that from mid-spring to mid-autumn in the afternoon the warmer water and the higher air temperature led to reduced RH and consequently to high Δe. This coincides with the diurnal high Ws which results not only in the daily maximum evaporation rate but also in a double peak mean diurnal evaporation cycle. Furthermore, this results in higher evaporation after maximum diurnal radiation. This timing of the diurnal maximum in the evaporative cooling effect has critical ramifications for the diurnal thermoregulation processes of shallow water, where coral reefs reside. The diurnal energy partitioning demonstrates how an increase in water temperature will be mitigated by evaporative cooling under the normal conditions of sustained daytime winds and extremely dry and hot air.

The strong evaporation enabled by the dry air overcoming the input of energy through the surface of the sea, resulting in a negative Q_{SWR} -79 W m^{-2}. Similar to the thermoregulation processes at the coral reef of the GoE (Abir et al., 2022) in the summer, the surface fluxes thermoregulate the shallow water temperature at the diurnal time scale. The water temperature reaches its maximum diurnal value shortly after peak radiation, 3 h before the Ta maximum diurnal value. The lag of air temperature after the water temperature is not intuitive, since the heat capacity of water is larger than the air's. This is caused by the strong evaporative cooling effect as indicated by the coincidence of the maximum daily Tw and the crossing of the Q_{SWR} to negative values in the afternoon.

7.3 Energy balance closure and advection term estimation

Throughout most of the 2-year observation period, the surface fluxes cool the surface water. Without the support of advected heat, the evaporation rate will decay due to the cooling of the water and decreased water vapor pressure, therefore this continuous high rate of evaporation can only be sustained with the advection of heat from the south (Biton & Gildor, 2011a).

During the winter, autumn, and summer campaigns, the heat storage was calculated based on temperature measurements of the top 145 m of the GoE. During winter when several hundred meters (>400 m (Shaked & Genin, 2022)) of the water column is mixed and the deficit to complete the energy balance closure could account for mainly two factors; cooling of the deeper water column (which was not measured) and heat transported by advection. During autumn due to the thermocline being deeper than our measurements of temperature (~200 m (Shaked & Genin, 2022)), the large deficit to the energy balance closure (174 W m^{-2}) is attributed to advection through the northern bound surface currents and cooling of the deeper water and deepening of the thermocline. During summer, when the shallow water is strongly stratified and the thermocline is ~100 m deep, and the net surface fluxes are relatively weak (7 W m^{-2}), the warming of the water is a direct result of heat advection from the south as Biton & Gildor (2011b) found. Therefore, concluding that the surface fluxes contribute to the heating processes of the surface water only at the diurnal scale and offer substantial cooling during the seasonal time scale.

7.4 Winter synoptic-scale forcing for high rates of heat loss

Wintertime synoptic scale variability in atmospheric circulation drives extreme rates of heat loss from the water of the GoE. Our direct flux measurements resolved the gap from previous studies, that utilized remote sensing data with larger pixel size than the GoE width (Menezes et al., 2019; Papadopoulos et al., 2013). The steep sea level pressure gradient over the Red Sea,

caused by the RST resulted in high wind speeds which are cold and dry leading to high rates of heat loss during winter. Cooling of the surface water by the daily mean rate of ~-500 W m^{-2} during the event, 2.5 times larger than the two years winter mean, increased the density of the surface water by increasing salinity through evaporation and by cooling. Thus, the cooling event impacted the vertical stability of the water column and enhances processes that lead to the annual winter vertical mixing processes. Indeed, the water column at the northern GoE was mixed during that winter (2021/2) to a depth greater than 700 m for the first time in a decade, where the mixing depth didn't exceed ~500 m. Additionally, supported by the number of large heat loss events during the winter (especially during December) before the deep mixing year and the shallow depth mixing year in our observation period (>700 and 450 m respectively). This relation of extreme surface heat losses, driven by synoptic-scale circulation, to winter water column mixing (basin overturning circulation), should be further explored as preconditioning events for winter water column mixing.

8 Conclusions

- Direct measurements for two years show a higher annual mean evaporation rate (3.22 m $year^{-1}$) in the GoE compared to lower indirect estimates using bulk formulae (1.6-1.8 m $year^{-1}$).
- Evaporation minimum occurs during winter due to a reduction in wind speed and the overall lower wind speed vapor pressure difference product.
- Higher rates of evaporation outside winter are a result of higher wind speed persisting throughout the afternoon into the evening as compared to winter. The higher winds coincide with the diurnal maximum in vapor pressure difference due to the afternoon decrease in relative humidity and the diurnal warming of the surface water.
- The current parametrization of the bulk formulae vapor transfer coefficient has large uncertainties in stable ABL environments. Concluding that the parametrization of the ABL stability and the calculation of the friction velocity should be revisited in environments such as the GoE. The vapor transfer coefficient derived from the EC is 0.00229, it applies to the northern GoE only.
- The surface energy exchange fluxes are mostly cooling the surface water. The minimal summer net gain in energy is not enough to explain the annual increase in water temperature entering the warm seasons.
- Advection fluxes bringing warmer water to the GoE are sustaining year-long high rates of evaporation, due to $\mathrm{LE} > \mathrm{RN} + \mathrm{SH}$.

- Winter synoptic scale events that force high rates of LE and SH loss from the sea to the ABL could be acting as preconditioning to deep vertical water column mixing in GoE.
- More accurate evaporation estimates should be used as input for ocean circulation modeling to revisit previous simulations of the GoE circulation which were based on bulk formulae estimation of evaporation.
- Future efforts in resolving the spatial distribution of the evaporation rate, ABL stability, and surface friction velocity at the GoE and the Red Sea should be a research priority. Specifically, how they change in response to winds being carried for longer distances over the narrow sea.

9 Appendix A

season	LE [W m-]	SH [W m-]	Ta [°C]	RH [%]	Tir [°C]	Tw [°C]	u [m s-1]	v [m s-1]	DLW [W	ULW [W	DSW [W
Annual											
max	1093	246	43.22	92	36.74	30.9	12.36	9.34	543	508	1078
min	-50	-249	9.07	6	13.37	19.07	-11.69	-8.12	259	376	-8
std	163	46	6.52	13	4.27	2.14	2.65	2.25	47	24	324
mean	255	-20	25.85	42	24.64	24.47	3.69	1.59	366	439	244
Autumn											
max	994	227	42.01	92	33.38	30.8	9.48	7.89	473	493	904
min	-50	-249	16.41	11	19.81	22.1	-7.27	-4.42	306	411	-3
std	157	37	4.5	12	2.15	1.35	2.3	2.33	28	13	287
mean	241	-22	27.78	47	25.92	26.11	3.81	2.15	381	447	212
Summer											
max	1093	244	43.22	84	36.74	30.9	9.7	9.34	543	508	1042
min	-49	-247	22.29	9	14.16	23.7	-5.56	-4.74	324	381	-8
std	158	42	3.4	12	2.42	1.48	2.52	2.74	40	13	376
mean	276	-49	32.06	39	29.28	26.33	3.62	1.66	412	465	318
Spring											
max	1070	246	42.24	82	35.24	26.1	12.36	6.92	506	505	1078
min	-46	-247	10.48	6	13.73	19.07	-7.71	-6.51	271	378	-8
std	173	47	5.74	13	3.51	0.95	2.76	1.75	34	20	349
mean	271	-25	24.71	37	23.09	22.45	4.34	1.24	346	430	279
Winter											
max	1014	205	28.05	88	26.63	25.37	10.45	7.03	477	451	890
min	-44	-239	9.07	15	13.37	21.1	-11.69	-8.12	259	376	0
std	161	29	3.32	12	2.14	0.96	2.81	1.93	29	12	242
mean	232	19	18.75	47	20.21	22.99	2.95	1.33	323	414	165

USW [W	RN [W m-	Δe	ΔT [°C]	Δe × Ws	ΔT × Ws	ET [mm	Q_{SWR} [W	Ws [m s-	Wd [°]	u* [m s-1]	z/L [-]
119	1031	31.89	7.07	244.64	44.17	37.77	946	13.34	37	4.17	86.42
-5	-147	1.83	-13.04	2.37	-99.26	-1.72	-1047	0.2	215	0.03	-96.02
17	316	3.38	2.63	38.33	14.26	5.65	284	2.4	40	0.13	0.97
16	155	16.13	-1.21	74.72	-6.88	8.82	-81	4.72	23	0.31	0.06
66	838	27.95	5.48	243.3	26.42	34.36	805	11.4	40	1.31	8.81
-3	-126	2.06	-13.04	2.9	-99.26	-1.72	-987	0.35	211	0.03	-25.5
17	277	3.51	2.63	38.1	15.89	5.43	239	2.44	45	0.11	0.52
17	129	15.86	-1.86	76.08	-10.45	8.34	-90	4.89	29	0.3	0.06
98	1020	31.89	1.5	244.64	7.4	37.77	919	11.93	44	4.17	86.42
-5	-118	4.26	-13.04	2.59	-93.46	-1.68	-978	0.2	220	0.03	-14.38
14	369	3.94	1.5	39.26	10.86	5.47	334	2.32	47	0.16	1.25
12	252	15.77	-2.78	76.55	-14.08	9.55	25	4.91	25	0.31	0.21
119	1031	27.19	4.47	226.88	22.85	36.96	946	12.98	29	2.36	7.67
-5	-131	1.83	-9.62	3.12	-65.6	-1.58	-1047	0.35	220	0.03	-96.02
17	337	3.01	2.39	39.03	13.02	5.97	297	2.51	32	0.14	1.38
17	179	15.58	-1.62	76.48	-8.21	9.35	-66	4.98	16	0.33	0.06
113	779	24.92	7.07	220.67	44.17	35.03	556	13.34	34	1.82	7.48
-5	-147	5.34	-4.47	2.37	-27.84	-1.54	-1033	0.3	215	0.04	-12.78
20	226	2.63	1.65	36.42	7.6	5.56	198	2.21	35	0.12	0.3
19	55	17.31	1.46	69.73	5.41	8.01	-195	4.11	24	0.31	-0.08

Table A1: Seasonal mean and the entire observation period statistics of micrometeorological and fluxes variables.

10 Appendix B

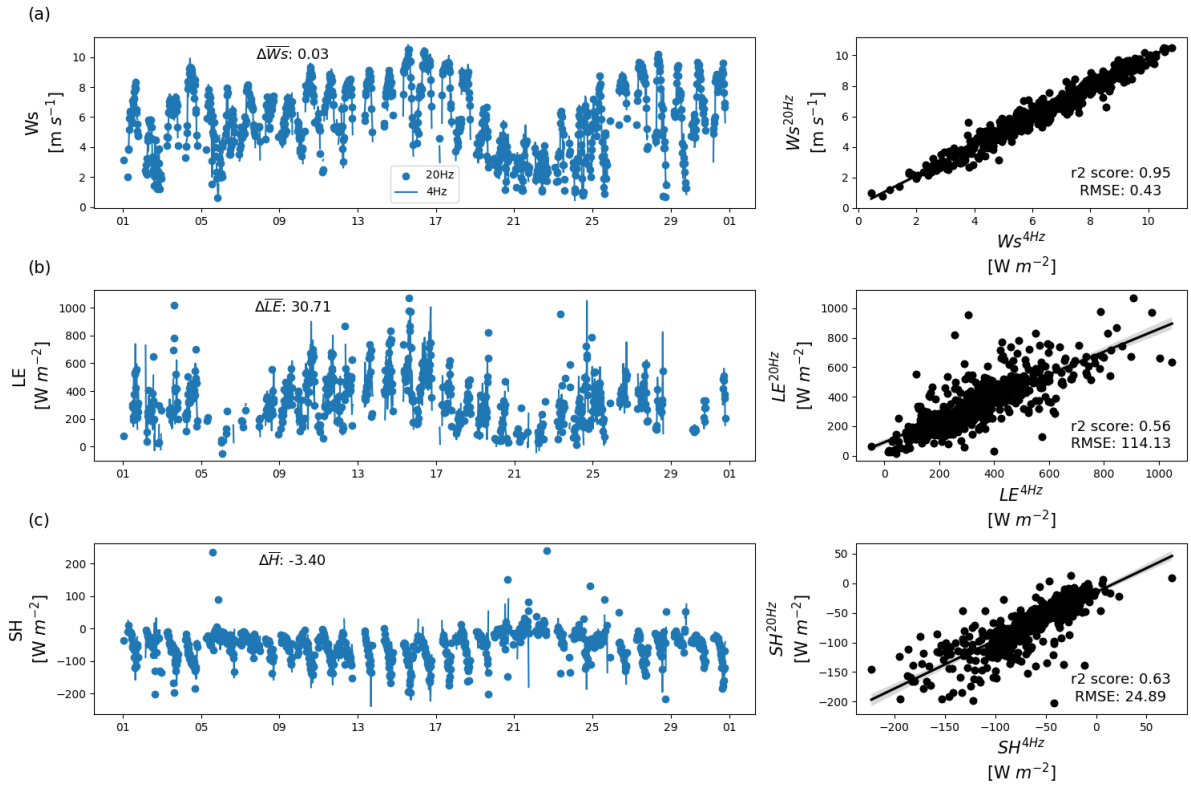

Figure B1: Comparison between the measured fluxes and artificially made downsampled raw EC data to 4 Hz to assess the uncertainty in the flux computation during the period that the station measured in 4 Hz due to an error (April-June 2022), time series (left) and scatter plot (right).

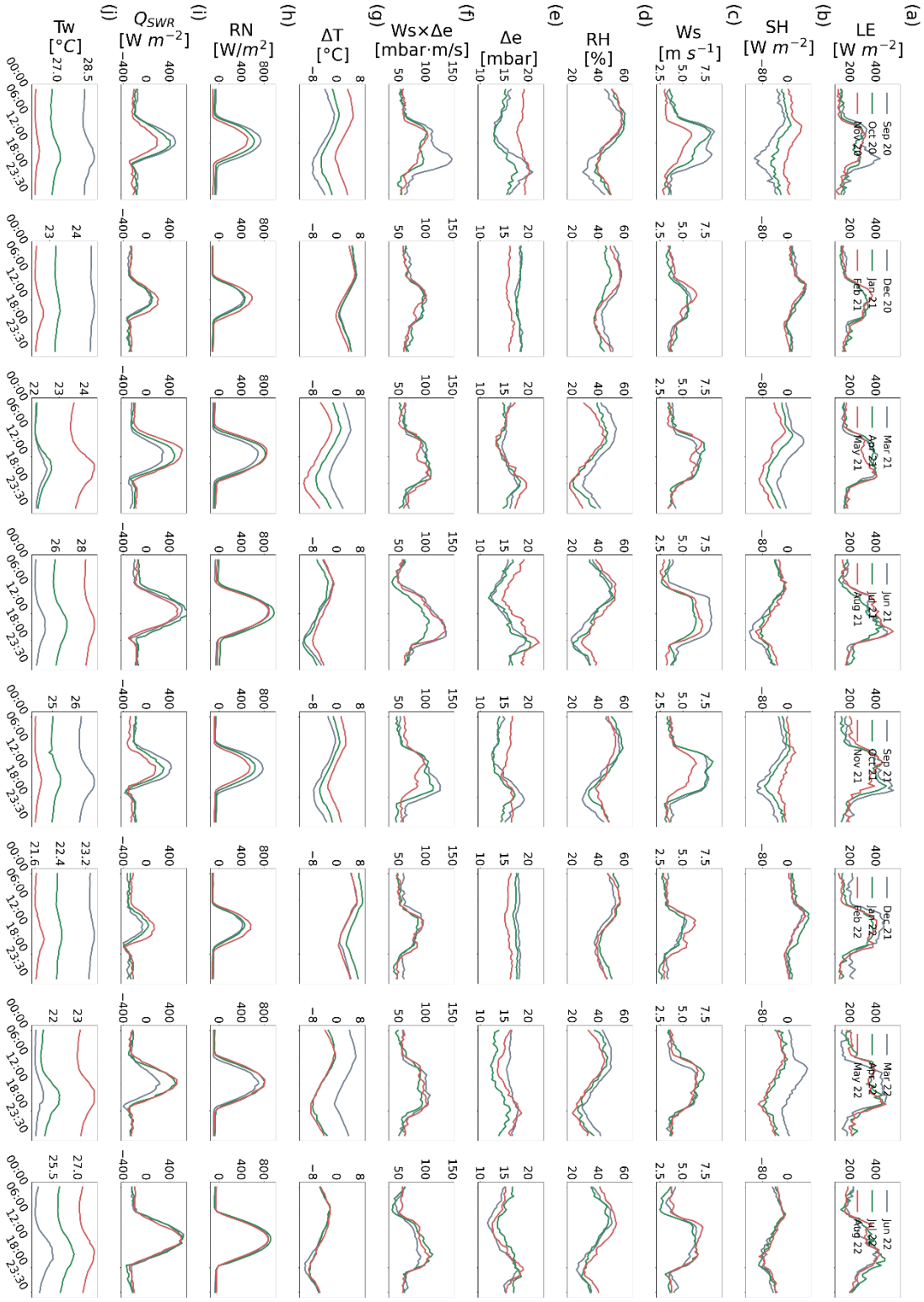

Figure B2: Monthly mean diurnal cycle of micrometeorological and flux variables divided into seasons (Winter=DJF, Spring=MAM, Summer=JJA, Autumn=SON). (a) Latent heat flux (LE), (b) Sensible Heat flux (SH), (c) Wind speed (Ws), (d) Relative humidity (RH), (e) Vapor pressure difference (Δe), (f) Wind speed and vapor pressure difference product (Ws × Δe), (g) water-air temperature difference (ΔT), (h) Net radiation (RN), (i) Sea water residual (Q_{SWR}) (j) Water temperature (Tw).

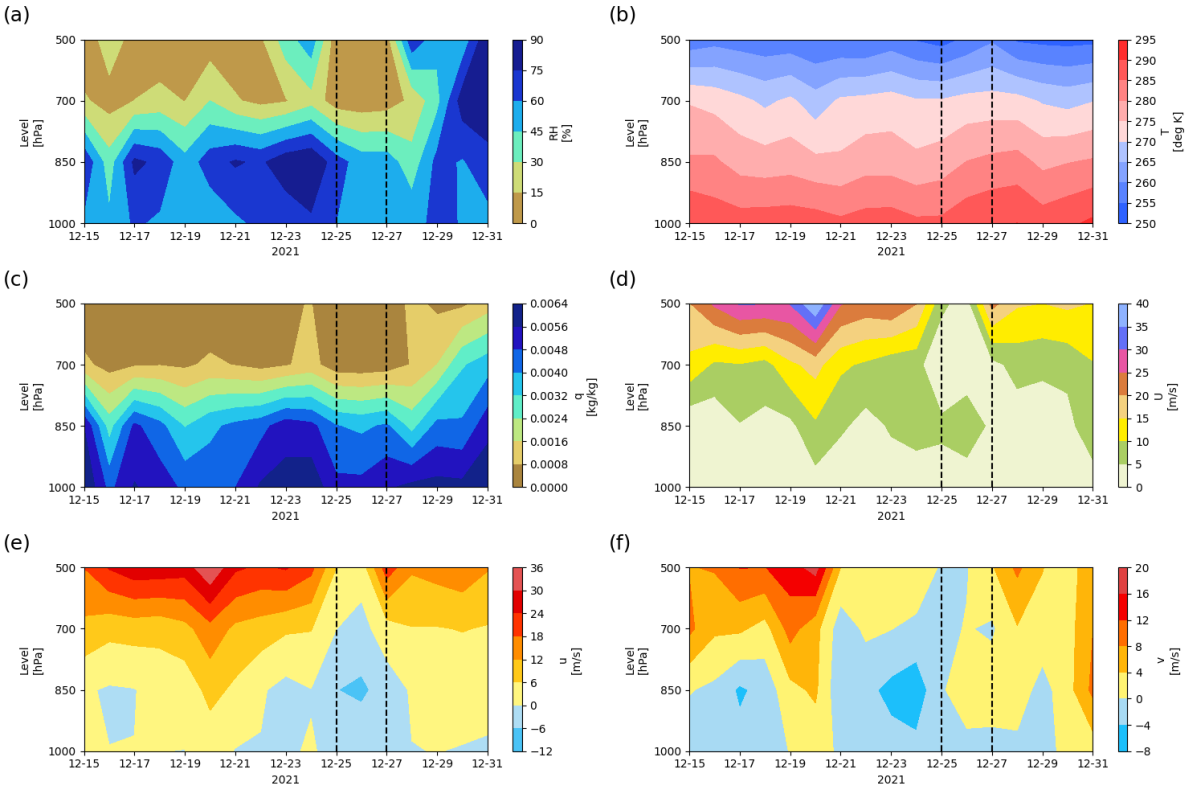

Figure B3: Vertical profile of the daily averaged ERA-5 pressure level hourly data (Hersbach et al., 2023b, 2023a) at the closest gridpoint to the IUI station (29N, 35E). (a) relative humidity, (b) air temperature, (c) specific humidity, (d) wind speed, (e) u-component of the wind, (f) v- component of the wind. The profiles show intensification of the western component of the winds specifically at 850 hPa, lower relative humidity values.

11 Appendix C: Evaluating how the travel distance of the winds over the sea effect heat exchange

To evaluate how the heat exchange will change along the GoE where in the southern areas the wind travels a longer distance over the sea; examining how the heat exchange varies in the rarer times where a synoptic state leads to southerly winds which travel a longer distance than the dominant northerly winds. This analysis is conducted in winter months (DJF) as southerly winds are more common in the winter season due to regional synoptic. When the wind is originated from the sea (135-260º), the wind speed is weaker by ~0.7 m s-1 however, with two times larger range of 1 SD (Fig S6). Relative humidity exhibits similar behavior but of an opposing trend- when the wind is sea-originated the relative humidity is higher (51% during the sea-originated direction in comparison to 47% during the northerly winds) due to the longer travel time over water. The lower wind speed and higher humidity result in an average reduction of 3 mbar and 33 W m-2 in the mean diurnal cycle of the vapor pressure difference and latent heat flux, respectively in the sea-originated wind occasions. The water and air temperature difference demonstrates a 3.35 ºC variation through the mean diurnal cycle with a mean temperature difference of 2.03 ºC. In comparison during normal flow days, the water and air temperature difference mean diurnal variations are in a magnitude of 6.06 ºC with a mean value of 4.36 ºC; which is a result of the higher air temperature in the sea-originated flow. Ultimately the dumping of the gradient and the weaker winds during sea-originated winds results in an average 21 W m-2 reduction in the mean diurnal cycle of the sensible heat.

When wind originates from the north the air temperature and relative humidity portrayed high diurnal variation which is more typical of terrestrial boundary layer characteristics (Pal Arya, 1988). When the wind was blowing from the south, air temperature and relative humidity had smaller diurnal variations, and the water-air temperature difference decreased. This reduces the sensible and latent heat fluxes at our measurements site. However, it is difficult to determine if there would be an actual significant reduction due to spatial wind speed variations throughout the GoE and the large overlap between the 1 SD range from the mean between the two flow types. Above the open sea and in the southern wider parts of the GoE wind speed increases (Berman et al., 2000) due to the lower roughness of the sea surface than the lands (Pal Arya, 1988). To resolve the spatial

distribution of heat fluxes multiple EC station comparison is needed or a Lagrangian approach of a vessel-mounted EC station.

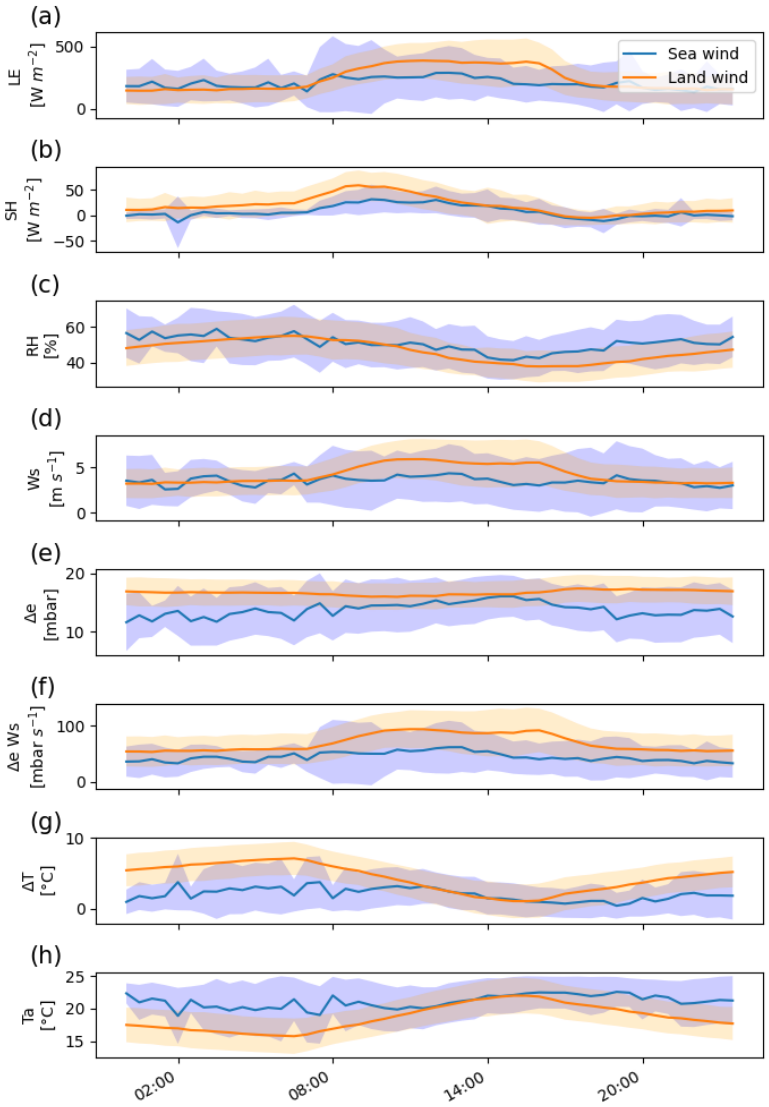

Fig C1. Comparison of the mean diurnal cycle of the heat fluxes and micrometeorology divided by sea-originating wind and land-origination wind (the shaded area corresponded to the +/- 1 sd.). Sea winds 135<= wind direction <=260 deg from the north (to compare southerly winds with long travel time over the sea) and the rest is land-originated wind (DJF only). (a) Latent heat, (b) sensible heat, (c) relative humidity, (d) wind speed, (e) vapor pressure difference, (f) vapor pressure difference and wind speed product, (g) water and air temperature difference, (h) air temperature.

12 Data availability statement

Datasets for this research are available in these in-text data citation references: Abir, S. (2023)

V1. https://doi.org/ 10.17632/wmtdmjgsfp.1.

The IUI monitoring program data used for this research are available at http://www.meteo-tech.co.il/eilat-yam/eilat_en.asp. The WireWalker CTD data is available upon request from Prof. Hezi Gildor: Hezi.gildor@mail.huj.ac.il

The ERA5 hourly data on a single level (Hersbach et al., 2023b) and pressure level (Hersbach et al., 2023a) in this study are available at https://cds.climate.copernicus.eu/cdsapp#!/dataset/reanalysis-era5-single-levels?tab=overview.

Software for this research is available in these in-text data citation references: LI-COR Biosciences. (2021). Eddy Covariance Processing Software (Version 7.0.8) [Software]. Available at www.licor.com/EddyPro.

13 References

Abir, S., McGowan, H. A., Shaked, Y., & Lensky, N. G. (2022). Identifying an Evaporative Thermal Refugium for the Preservation of Coral Reefs in a Warming World—The Gulf of Eilat (Aqaba). Journal of Geophysical Research: Atmospheres, 127(24). https://doi.org/10.1029/2022JD036845

Abir, S., McGowan, H., Shaked, Y., Morin, E., & Lensky, N. (2023). 2 years Eddy Covariance measurements over the Gulf of Eilat (Aqaba), V1 [Dataset]. Mendeley Data. https://doi.org/10.17632/wmtdmjgsfp.1

Afargan, H., & Gildor, H. (2015). The role of the wind in the formation of coherent eddies in the Gulf of Eilat/Aqaba. Journal of Marine Systems, 142, 75–95. https://doi.org/10.1016/j.jmarsys.2014.09.006

Alpert, P., Osetinsky, I., Ziv, B., & Shafir, H. (2004). Semi-objective classification for daily synoptic systems: Application to the eastern Mediterranean climate change. International Journal of Climatology, 24(8), 1001–1011. https://doi.org/10.1002/joc.1036

Assaf, G., & Kessler, J. (1976). Climate and energy exchange in the Gulf of Aqaba (Eilat). Monthly Weather Review.

Bardal, L. M., Onstad, A. E., Sætran, L. R., & Lund, J. A. (2018). Evaluation of methods for estimating atmospheric stability at two coastal sites. Wind Engineering, 42(6), 561–575. https://doi.org/10.1177/0309524X18780378

Ben-Sasson, M., Brenner, S., & Paldor, N. (2009). Estimating air-sea heat fluxes in semienclosed basins: The case of the Gulf of Elat (Aqaba). Journal of Physical Oceanography, 39(1), 185–202. https://doi.org/10.1175/2008JPO3858.1

Berman, T., Paldor, N., & Brenner, S. (2000). Simulation of wind-driven circulation in the Gulf of Elat Aqaba. Journal of Marine Systems (Vol. 26). Retrieved from www.elsevier.nlrlocaterjmarsys

Berman, T., Paldor, N., & Brenner, S. (2003). The seasonality of tidal circulation in the Gulf of Elat. Israel Journal of Earth Sciences, 52(1), 11–19. https://doi.org/10.1560/G72J-CYHM-D202-FJY2

Bignami, F., Marullo, S., Santoleri, R., & Schiano, M. E. (1995). Longwave radiation budget in the Mediterranean Sea. Journal of Geophysical Research, 100(C2), 2501–2514. https://doi.org/10.1029/94JC02496

Biton, E., & Gildor, H. (2011a). Stepwise seasonal restratification and the evolution of salinity minimum in the Gulf of Aqaba (Gulf of Eilat). Journal of Geophysical Research: Oceans, 116(8). https://doi.org/10.1029/2011JC007106

Biton, E., & Gildor, H. (2011b). The general circulation of the Gulf of Aqaba (Gulf of Eilat) revisited: The interplay between the exchange flow through the Straits of Tiran and surface fluxes. Journal of Geophysical Research: Oceans, 116(8). https://doi.org/10.1029/2010JC006860

Dayan, U., Tubi, A., & Levy, I. (2012). On the importance of synoptic classification methods with respect to environmental phenomena. International Journal of Climatology, 32(5), 681–694. https://doi.org/10.1002/joc.2297

Edson, J., Crawford, T., Crescenti, J., Farrar, T., Frew, N., Gerbi, G., et al. (2007). The Coupled Boundary Layers and Air-sea Transfer Experiment in Low Winds.

Eshel, G., & Heavens, N. (2007). Climatological evaporation seasonality in the northern Red Sea. Paleoceanography, 22(4). https://doi.org/10.1029/2006PA001365

Fairall, C. W., Bradley, E. F., Rogers, D. P., Edson, J. B., & Young, G. S. (1996). Bulk parameterization of air-sea fluxes for tropical ocean-global atmosphere coupled-ocean atmosphere response experiment. Journal of Geophysical Research: Oceans, 101(C2), 3747–3764. https://doi.org/10.1029/95JC03205

Foken, T., Göckede, M., Mauder, M., Mahrt, L., Amiro, B., & Munger, W. (2004). Hand book of Micromereotology post-field data quality control (pp. 181–208).

Genin, A., Levy, L., Sharon, G., Raitsos E, D. E., & Diamant, A. (2020). Rapid onsets of warming events trigger mass mortality of coral reef fish. PNAS. https://doi.org/10.1073/pnas.2009748117/-/DCSupplemental

Gutiérrez-Loza, L., & Ocampo-Torres, F. J. (2016). Air-sea CO2 fluxes measured by eddy covariance in a coastal station in Baja California, México. In IOP Conference Series: Earth and Environmental Science (Vol. 35). Institute of Physics Publishing. https://doi.org/10.1088/1755-1315/35/1/012012

Hamdani, I., Assouline, S., Tanny, J., Lensky, I. M., Gertman, I., Mor, Z., & Lensky, N. G. (2018). Seasonal and diurnal evaporation from a deep hypersaline lake: The Dead Sea as a case study. Journal of Hydrology, 562, 155–167. https://doi.org/10.1016/j.jhydrol.2018.04.057

Hersbach, H., Bell, B., Berrisford, P., Biavati, G., Horányi, A., Muñoz Sabater, J., et al. (2023a). ERA5 hourly data on pressure levels from 1940 to present. Copernicus Climate Change Service (C3S) Climate Data Store (CDS). https://doi.org/10.24381/cds.68d2bb30

Hersbach, H., Bell, B., Berrisford, P., Biavati, G., Horányi, A., Muñoz Sabater, J., et al. (2023b). ERA5 hourly data on single levels from 1940 to present. Copernicus Climate Change Service (C3S) Climate Data Store (CDS).

Israel Meteorological Service. (2023). Eilat annual average precipitation. Retrieved June 13, 2023, from https://ims.gov.il/he/ClimateAtlas

Klinker, J., Reiss, Z., Kropach, C., Levanon, I., Harpaz, H., Halicz, E., & Assaf, G. (1976). Observations on the Circulation Pattern in the Gulf of Elat ('Aqaba), Red Sea. Israel Journal of Earth Sciences, 25, 85–103.

Kondo, J. (1975). Air-sea Bulk Transfer Coefficient in Diabatic Conditions. Boundary-Layer Meteorology, 9, 91–112. https://doi.org/https://doi.org/10.1007/BF00232256

Lensky, N. G., Lensky, I. M., Peretz, A., Gertman, I., Tanny, J., & Assouline, S. (2018). Diurnal Course of Evaporation From the Dead Sea in Summer: A Distinct Double Peak Induced by Solar Radiation and Night Sea Breeze. Water Resources Research, 54(1), 150–160. https://doi.org/10.1002/2017WR021536

LI-COR Biosciences. (2021). EddyPro® Software v7.0. Retrieved from https://www.licor.com/env/support/EddyPro/software.html

LI-COR Biosciences. (2023). EddyPro® 7 Software: Express default settings. Retrieved June 13, 2023, from https://www.licor.com/env/support/EddyPro/topics/express-defaults.html

MacKellar, M. C., & McGowan, H. (2010). Air-sea energy exchanges measured by eddy covariance during a localised coral bleaching event, Heron Reef, Great Barrier Reef, Australia. Geophysical Research Letters, 37(24). https://doi.org/10.1029/2010GL045291

Mahabbati, A., Beringer, J., Leopold, M., McHugh, I., Cleverly, J., Isaac, P., & Izady, A. (2021). A comparison of gap-filling algorithms for eddy covariance fluxes and their drivers. Geoscientific Instrumentation, Methods and Data Systems, 10(1), 123–140. https://doi.org/10.5194/gi-10-123-2021

McGowan, H., Sturman, A. P., MacKellar, M. C., Wiebe, A. H., & Neil, D. T. (2010). Measurements of the local energy balance over a coral reef flat, Heron Island, southern Great Barrier Reef, Australia. Journal of Geophysical Research Atmospheres, 115(19). https://doi.org/10.1029/2010JD014218

McGowan, H., Sturman, A., Saunders, M., Theobald, A., & Wiebe, A. (2019, April 27). Insights From a Decade of Research on Coral Reef—Atmosphere Energetics. Journal of Geophysical Research: Atmospheres. Blackwell Publishing Ltd. https://doi.org/10.1029/2018JD029830

Menezes, V. V., Farrar, J. T., & Bower, A. S. (2019). Evaporative Implications of Dry-Air Outbreaks Over the Northern Red Sea. Journal of Geophysical Research: Atmospheres, 124(9), 4829–4861. https://doi.org/10.1029/2018JD028853

Mor, Z., Assouline, S., Tanny, J., Lensky, I. M., & Lensky, N. G. (2018). Effect of Water Surface Salinity on Evaporation: The Case of a Diluted Buoyant Plume Over the Dead Sea. Water Resources Research, 54(3), 1460–1475. https://doi.org/10.1002/2017WR021995

Morin, T. H., Bohrer, G., Naor-Azrieli, L., Mesi, S., Kenny, W. T., Mitsch, W. J., & Schäfer, K. V. R. (2014). The seasonal and diurnal dynamics of methane flux at a created urban wetland. Ecological Engineering, 72, 74–83. https://doi.org/10.1016/j.ecoleng.2014.02.002

Pal Arya, S. (1988). Introduction to micrometeorology. Academic Press, Inc.

Papadopoulos, V. P., Abualnaja, Y., Josey, S. A., Bower, A., Raitsos, D. E., Kontoyiannis, H., & Hoteit, I. (2013). Atmospheric forcing of the winter air-sea heat fluxes over the northern red sea. Journal of Climate, 26(5), 1685–1701. https://doi.org/10.1175/JCLI-D-12-00267.1

Paynes, R. E. (1972). Albedo of the sea surface. Journal of Atmospheric Sciences, 959–970. https://doi.org/https://doi.org/10.1175/1520-0469(1972)029<0959:AOTSS>2.0.CO;2

Pérez, A., Lagos, O., Lillo-Saavedra, M., Souto, C., Paredes, J., & Arumí, J. L. (2020). Mountain lake evaporation: A comparative study between hourly estimations models and in situ measurements. Water (Switzerland), 12(9). https://doi.org/10.3390/w12092648

Pivato, M., Carniello, L., Gardner, J., Silvestri, S., & Marani, M. (2018). Water and sediment temperature dynamics in shallow tidal environments: The role of the heat flux at the sediment-water interface. Advances in Water Resources, 113, 126–140. https://doi.org/10.1016/j.advwatres.2018.01.009

Rey-Sánchez, A. C., Bohrer, G., Morin, T. H., Shlomo, D., Mirfenderesgi, G., Gildor, H., & Genin, A. (2017). Evaporation and CO2 fluxes in a coastal reef: an eddy covariance approach. Ecosystem Health and Sustainability, 3(10). https://doi.org/10.1080/20964129.2017.1392830

Santini, M. F., Souza, R. B., Pezzi, L. P., & Swart, S. (2020). Observations of air–sea heat fluxes in the southwestern Atlantic under high-frequency ocean and atmospheric perturbations.

Quarterly Journal of the Royal Meteorological Society, 146(733), 4226–4251. https://doi.org/10.1002/qj.3905

Shaked, Y., & Genin, A. (2022). Scientific report 2021. Eilat. Retrieved from http://www.iui-eilat.ac.il/NMP

Shalev, E., Lyakhovsky, V., Weinstein, Y., & Ben-Avraham, Z. (2013). The thermal structure of Israel and the Dead Sea Fault. Tectonophysics, 602, 69–77. https://doi.org/10.1016/j.tecto.2012.09.011

Sofianos, S. S., Johns, W. E., & Murray, S. P. (2002). Heat and freshwater budgets in the Red Sea from direct observations at Bab el Mandeb. Deep-Sea Research II (Vol. 49).

Sverdrup, H. U., Johnson, M. W., & Fleming, R. H. (1942). The Oceans, Their Physics, Chemistry, and General Biology. New York: Prentice-Hall.

Tau, G., Enzel, Y., McGowan, H., Lyakhovsky, V., & Lensky, N. G. (2022). Air-water interactions regulating water temperature of lakes: Direct observations (Agamon Hula, Israel) and analytical solutions. Journal of Hydrology, 614, 128515. https://doi.org/10.1016/J.JHYDROL.2022.128515

Yu, L. (2018). Global Air-Sea Fluxes of Heat, Fresh Water, and Momentum: Energy Budget Closure and Unanswered Questions. Annual Review of Marine Science, 11, 227–248. https://doi.org/10.1146/annurev-marine-010816

מחקר על חילוף החום, גז ומומנטום בין הים לאטמוספירה באמצעות שטפי פני שטח, מספק תובנות חשובות לגבי התהליכים הפיזיקליים והכימיים של סביבות ימיות. שטפי חילוף החום אלו משפיעים על האקלים, תהליכי סירקולציה של האוקיינוסים ותהליכי תרמו-רגולציה של הסביבה הביולוגית הימית.

מטרת מחקר זה היא לכמת במדויק את שטפי חילוף החום במפרץ אילת. בנוסף, לקבוע את קצב האידוי כתגובה למיקרו-מטאורולוגיה, ובפרט לנתח את הקשר בין מהירות הרוח, הפרש לחצי האדים, קצבי האידוי והמחזורים היומיים והעונתיים שלהם. המחקר גם בוחן את השגיאה בנוסחאות 'bulk formulae' לאידוי תחת תנאי אטמוספירה יציבים במפרץ אילת. בנוסף, המחקר מעריך את חילופי האנרגיה נטו ומאזן החום של מי פני השטח ועמודת המים, ובוחן את התרומה של הסעת חום על ידי הזרמים למאזן החום הכולל, המספקים תובנות לגבי הדינמיקה של מפרץ אילת. המחקר גם בוחן את ההשפעה של הסירקולציה הסינופטית בחורף על איבוד חום מפני השטח של המים והערבוב האנכי של עמודי המים במפרץ אילת.

כדי להשיג יעדים אלה, נערך מחקר בן שנתיים תוך שימוש במדידות אדי קוריאנס של שטפי החום בין הים לאטמוספירה במפרץ אילת. גישת מאזן האנרגיה הופעלה כדי לכמת את חלוקת אנרגיית המלאה בין הים לאטמוספירה ועמודת המים.

הממצאים מצביעים על כך שקצב האידוי הממוצע במפרץ אילת הוא 3.22 מ' לשנה; קצב העולה על הערכות קודמות שנגזרו מנוסחאות 'bulk formulae' ושטף חום המסופק על ידי הקרינה לים באקלים מדברי. הפרמטריזציה של יציבות שכבת הגבול האטמוספירית מזוהה כגורם העיקרי לשגיאה בהערכת קצב האידוי בתנאי אטמוספירה יציבים. שיא קצב האידוי נמדד במהלך הקיץ, בניגוד להערכות קודמות שהעריכו שיא אידוי בחורף. קצב האידוי הנמוך ביותר מתרחש במהלך החורף (8.01 מ"מ ליום) כתוצאה מהפחתה במהירות הרוח. לעומת זאת, מהירויות רוח גבוהות יותר במהלך האביב, הקיץ והסתיו, המלוות בעלייה אחר הצהריים בהפרשי לחצי האדים עקב טמפרטורת מים גבוהה יותר ולחות יחסית נמוכה יותר, מביאות לקצב אידוי ממוצע גבוה יותר של 9.08 מ"מ ליום.

ניתוח הנתונים מראה כי ישנה השפעת קירור נטו על מי פני השטח (79- וואט למטר מרובע) בעיקר באמצעות אידוי לאורך רוב השנה, עם תוספת אנרגיה נטו קטנה שנצפתה במהלך הקיץ. הממצאים מצביעים על כך ששטף חום בין הים לאטמוספירה לבדו אינו יכול להסביר את החימום העונתי של מי המפרץ, כפי שצוין במחקרים קודמים. הגירעון המשמעותי בחום מפוצה על ידי חום המוסע דרך זרמים מהים האדום, רכיב המכומת בעקיפין באמצעות שיקולי איזון אנרגיה.

יתרה מכך, המחקר מספק הבנה מעמיקה יותר של הסקאלה הסינופטית המאלצת את חילוף האנרגיה בין הים לאטמוספירה באמצעות אירועי איבוד חום קיצוניים. אירועים אלו מצננים את מי פני השטח באופן משמעותי ומגבירים את מליחותם באמצעות אידוי וחום מוחשי, ובהתאם לכך מערערים את יציבות עמודת המים. חלק זה מעיד על חשיבותם של תהליכים אלו לערבוב אנכי של עמודת המים בחורף במפרץ אילת.

המכון הגיאולוגי
משרד האנרגיה

חילופי חום וגז בין הים לאטמוספירה במפרץ אילת (עקבה)

שי אביר

חיבור לשם קבלת התואר "מוסמך במדעי הטבע"

הוגש לאוניברסיטה העברית בירושלים.

העבודה נעשתה בהדרכתם של:

פרופ' נדב לנסקי, המכון הגיאולוגי לישראל
פרופ' אפרת מורין, האוניברסיטה העברית בירושלים
פרופ' היימיש מקגואוון, אוניברסיטת קווינס-לנד

דוח מס' GSI/11/2023 אוגוסט 2023

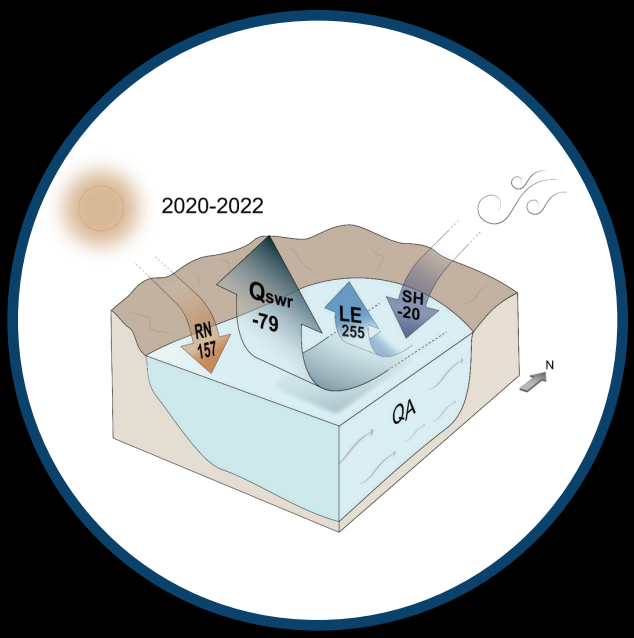
2020-2022
Qswr
-79
LE
255
SH
-20
RN
157
QA
N




0
50
100 m